Quantum states and intertwining phases in kagome materials

Wang, Yaojia; Wu, Heng; McCandless, Gregory T.; Chan, Julia Y.; Ali, Mazhar N.

DOI
10.1038/s42254-023-00635-7

Publication date
2023

Document Version
Final published version

Published in
Nature Reviews Physics

nature reviews physics

https://doi.org/10.1038/s42254-023-00635-7

Review article

Check for updates

Quantum states and intertwining phases in kagome materials

Yaojia Wang [1,2,4] ✉, Heng Wu [1,2,4], Gregory T. McCandless[3], Julia Y. Chan[3] & Mazhar N. Ali[1,2] ✉

Abstracts

In solid materials, non-trivial topological states, electron correlations and magnetism are central ingredients for realizing quantum properties, including unconventional superconductivity, charge and spin density waves and quantum spin liquids. The kagome lattice, made up of corner-sharing triangles, can host these three ingredients simultaneously and has proved to be a fertile platform for studying diverse quantum phenomena including those stemming from the interplay of these ingredients. This Review introduces the fundamental properties of the kagome lattice and discusses the complex phenomena observed in several materials systems, including the intertwining of charge order and superconductivity in some kagome metals, the modulation of magnetism and topology in some kagome magnets, and the combination of symmetry breaking and Mott physics in 'breathing' kagome insulators. The Review also highlights open questions in the field and future research directions in kagome systems.

Sections

[1]Kavli Institute of Nanoscience, Delft University of Technology, Delft, The Netherlands. [2]Department of Quantum Nanoscience, Faculty of Applied Sciences, Delft University of Technology, Delft, The Netherlands. [3]Department of Chemistry and Biochemistry, Baylor University, Waco, TX, USA. [4]These authors contributed equally: Yaojia Wang, Heng Wu. ✉e-mail: whyjwang@gmail.com; maz@berkeley.edu

Key points

- The kagome lattice is formed by corner-sharing triangles, which can host Dirac points, van Hove singularities (vHSs) and flat bands.
- The high Fermi surface instability around the vHSs and flat bands can give rise to various physical properties that can be entangled, including superconductivity, charge or spin orders, and complex magnetism.
- Charge density wave (CDW) states induced by the vHSs mostly appear in kagome materials with non-magnetic or weak magnetism, but are rare in kagome magnets. The relationship between magnetism and CDWs is not yet fully understood.
- Diverse magnetic properties appearing in kagome magnets are influenced by the interlayer and intralayer magnetic interaction of kagome lattices and other sublattices.
- A Mott-insulating state was observed in the symmetry breaking, breathing kagome insulators with flat bands. Strong correlation physics related to flat bands can be studied in kagome system.

Introduction

In solid state systems, basic electronic states such as metallic and semiconducting or insulating behaviour have been well described by free or nearly free electron theory based on non-interacting electrons in a periodic lattice potential. For correlated systems, however, where the Coulomb interaction cannot be ignored and is comparable to or stronger than the kinetic energy of the electrons, the interaction between particles (electron–electron and electron–phonon interactions) plays an important role in the material's physical properties. Electron correlation can induce instabilities at the Fermi surface and drive electronic fluctuations, leading to many new quantum phases with broken symmetry (Box 1), including superconductivity, complex magnetism, charge density waves (CDW), spin density waves (SDW), nematic and smectic orders, pair density waves (PDW)[1–4], Mott-insulating behaviour and more. These phases have been observed in strongly correlated systems, such as heavy fermion materials, high-temperature superconductors, complex oxide perovskites, transition metal dichalcogenides and twisted graphene[3,5–8]. However, they need not be distinct; these phases can compete and even become entangled with each other in the same material. This is the case in the cuprate superconductors where superconductivity competes with CDW and SDW phases, and an observed PDW phase is proposed to be the possible 'mother phase'[1]. The intertwining and interdependency of the different phases is complex, but eventual understanding may lead to insight into exotic physical properties, such as unconventional superconductivity.

One important structure type where this intertwining and interdependency is seen is in the kagome lattice, also known as the trihexagonal tiling. It is composed of hexagons that are surrounded by six equilateral triangles, each triangle corner-sharing with three other triangles (Fig. 1a). It naturally hosts geometrical frustration due to its triangular nature which, for example, causes magnetic frustration in kagome magnets like herbertsmithite[9,10], and has been predicted to give rise to a valence-bond state[11] and a strongly correlated quantum spin liquid state[12]. Additionally, the electronic interference between the three sublattices in the kagome net yields many electronic-band-structure features including topological Dirac, Weyl and nodal line points, van Hove singularities (vHSs) and flat bands. The vHSs and flat bands possess high densities of states, enhanced effective masses and strong electron–electron correlations. Hence, kagome materials are ideal for studying the interplay of topology, magnetism and electron correlation.

Early studies of kagome metals have found diverse phenomena, such as Weyl states in the ferromagnet $Co_3Sn_2S_2$ (refs. 13,14), Dirac points and flat bands in FeSn (ref. 15) (antiferromagnet) and CoSn (paramagnet) (refs. 16,17), signs of magnetic skyrmions in the non-collinear ferromagnet Fe_3Sn_2 (refs. 18,19), chiral spin structures in the non-collinear antiferromagnet Mn_3X (X = Sn, Ge)[20,21], and large anomalous Hall effects in many of these magnets[22,23]. The study of these kagome magnets and developments in understanding their physical properties have been reviewed[23–25]. More recently, several new materials systems have been found that host both distinct quantum phases and topological states, as well as the entanglement of these different states. For example, the topological kagome metals AV_3Sb_5 (A = K, Cs, Rb)[26–29] have attracted attention due to the observation of superconductivity, CDW, nematic and stripe order, PDW phase[30–33], and large anomalous Hall effect[34–36] all in a single material. These complex symmetry-breaking ordered states either compete or intertwine with each other, much like the situation of the high-temperature superconductors, but from a likely different origin; the early works in AV_3Sb_5 was introduced in some reviews[27–29]. Beyond AV_3Sb_5, new physical properties and possibilities are being explored in metallic kagome magnets like the AM_6X_6 (for instance, $TbMn_6Sn_6$)[37,38] family (the '166' compounds). These compounds have large chemical tunability and show an array of magnetic phases unlike the AV_3Sb_5 family, which does not exhibit long-range magnetic order. In addition, a new family of kagome insulators, Nb_3X_8 (X = Cl, Br, I), which has a trigonally distorted kagome lattice (that is, it has a breathing mode), are proposed to be possible Mott insulators and obstructed atomic insulators[39–42].

This Review introduces the diversity and state-of-the-art of the complex physical studies in contemporary kagome materials, some of which are the subject of debate and controversy. First, we discuss the basic physical concepts in kagome lattices and their corresponding quantum phenomena, then dive into detailed discussions of the aforementioned representative materials systems with different kinds of properties, particularly the AV_3Sb_5, '166' (including '0.5–3–3' compounds) and Nb_3X_8 families. The intertwining of charge orders and the superconducting state, with controversial studies of the physical mechanisms behind these phases, will be discussed for AV_3Sb_5. The discussion of AM_6X_6 family will focus on the magnetic phases and the modulation of magnetism under the influence of both interlayer and intralayer magnetic coupling. Additionally, the new topological states based on the combination of magnetism and topology and a structural transition with possible CDW states will be discussed. Finally, distinct from the topological kagome metals, new properties in the breathing kagome insulators will be introduced for Nb_3X_8, including a Mott-insulating state with an isolated flat band and a theorized obstructed atomic insulating state. The properties of different materials are compared in Table 1.

The kagome lattice and basic physical properties

The kagome lattice is made up of corner-sharing triangles (Fig. 1a), in which there are three sublattice sites per unit cell (labelled as A, B, C sites). These sites induce a high degree of geometrical frustration from balanced exchange for electron hopping between the different atoms.

Box 1

Electron-correlation-related quantum phases

- **Charge density wave (CDW) order:** a charge order that breaks translational symmetry. It normally causes a periodic lattice distortion due to electron–phonon coupling in systems with Fermi surface nesting (large, parallel sections of a Fermi surface that share a single vector in momentum space) and results in a splitting of energy states (in other words, a gap opening at the Fermi level) that lowers the ground-state energy[2,315]. Unconventional CDW mechanisms are also proposed in some 2D and 3D materials (such as $TiSe_2$), driven by an exitonic insulator mechanism or a band Jahn–Teller effect[2].
- **Spin density wave (SDW) order:** These share many similarities with CDW order, including the breaking of translational symmetry and Fermi surface nesting, but arise from a periodic modulation of the spin density (rather than the charge density) and occur because of electron–electron interactions[316].
- **Nematic and smectic phases:** A nematic phase spontaneously breaks only rotational symmetry and tends to have orientational ordering; a smectic phase is a unidirectional stripe-like phase that breaks rotational symmetry as well as translational symmetry along one direction[317,318].
- **Pair density wave (PDW) phase:** a special superconducting state in which the amplitude of the superconducting pairing oscillates periodically in space so that the spatial average of the superconducting order vanishes[319]. It is expected to arise where superconductivity coexists with CDW or SDW order.

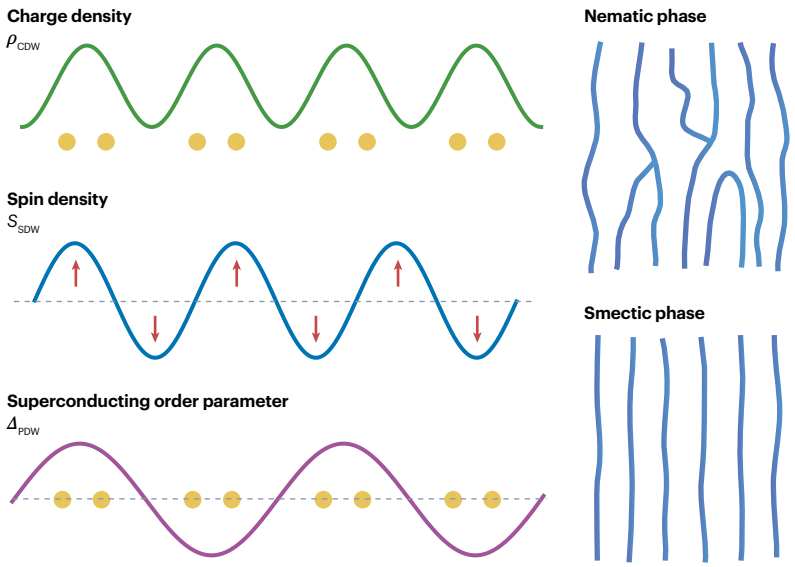

The electron interactions in the kagome lattice can be described with a Hubbard model, and the typical Hamiltonian takes the form[43,44]

$$H = H_0 + H_{\text{int}}$$

$$H_0 = -\sum_{\langle i,j\rangle\sigma} (t_{ij}\hat{c}^{+}_{i\sigma}\hat{c}_{j\sigma} + \text{h.c.}) - \mu\sum_{i,\sigma} n_{i,\sigma}$$

$$H_{\text{int}} = U_0\sum_i n_{i\uparrow}n_{i\downarrow} + \frac{U_1}{2}\sum_{\langle i,j\rangle,\sigma,\sigma'} n_{i,\sigma}n_{j,\sigma'}$$

where H_0 is the Hamiltonian from the tight-binding model including electron hopping and the chemical potential (μ). t_{ij} is the hopping integral and represents the kinetic energy of electrons hopping between nearest-neighbour sites. $\hat{c}_{i\sigma}$ and $\hat{c}^{+}_{i\sigma}$ are the annihilation and creation operators of electrons on the i site with spin σ, respectively, and $n_{i,\sigma} = \hat{c}^{+}_{i\sigma}\hat{c}_{i\sigma}$. H_{int} is the Hamiltonian considering the on-site (local) Hubbard interaction of scale U_0 (local interaction), and nearest-neighbour Coulomb interaction of scale U_1. Longer-range interactions (such as next-nearest-neighbour interactions) can also be included in some systems.

Without including electron interactions and symmetry-breaking distortions, the band structure of the ideal kagome lattice (in which t_{ij} is the same for nearest-neighbour sites in upward and downward triangles) based on a tight bonding model (H_0 part) shows the typical features of: a dispersionless flat band located at an energy of $2t$ and connected with the quadratic bands; a Dirac point around the K point; and two vHSs with logarithmic divergence located at the M point with different energy ($E = 0$ and $E = -2t$)[43–45] (Fig. 1d). The density of states (DOS) and electron effective mass at the Fermi level are highly elevated near the flat band and vHSs, where the strong correlation of the electrons needs to be considered (Fig. 1d). In the following, we discuss three band properties associated with the kagome lattice, and the influence of other factors on those bands and their corresponding physical properties.

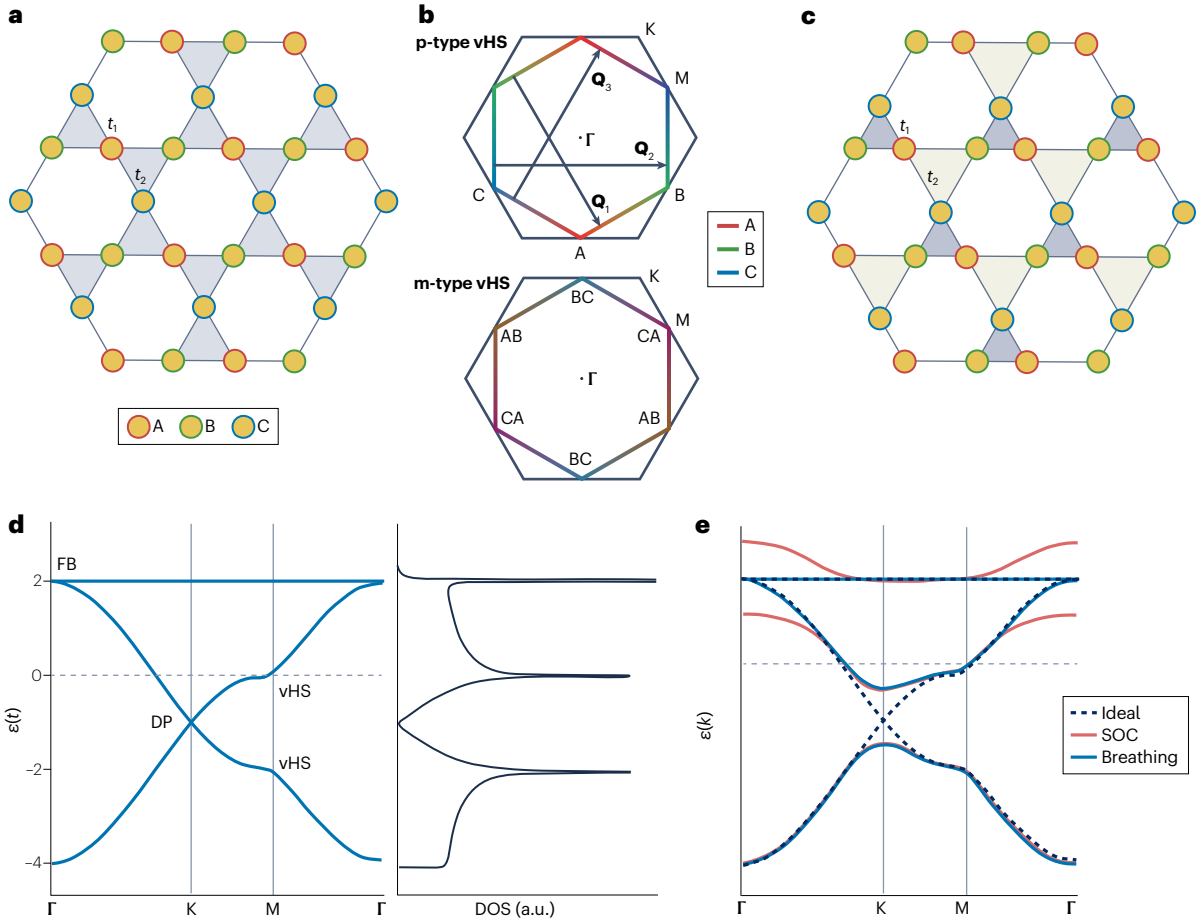

Fig. 1 | Lattice structure and electronic band property of kagome lattice. **a**, Structure of the ideal kagome lattice with hopping amplitude t_1 in the upward triangle equal to hopping amplitude t_2 in the downward triangle. A, B and C are three sites in the unit cell. **b**, Schematic of the Fermi surfaces in the hexagonal Brillouin zone. Two kinds of van Hove singularities (vHSs) with distinct sublattice decoration: the p-type vHS is sublattice-pure at the M point, whereas the m-type vHS has mixed sublattice features at the M point. Taking p-type vHS as an example, the Fermi surfaces are nested by three ordering wave factors Q_i, $i = 1,2,3$. **c**, Structure of breathing kagome lattice, in which $t_1 \neq t_2$. **d**, Band structure of ideal kagome lattice and corresponding density of states (DOS). The two vHSs, Dirac point (DP) and flat band (FB) are labelled. **e**, Band structures for ideal kagome lattice (black dashed line), and influence of spin–orbit coupling (SOC) and breathing kagome lattices. Part **e** adapted with permission from ref. 47, APS.

Topological states

The kagome lattice bands can be modulated by the effect of spin–orbit coupling (SOC), symmetry breaking and electron interaction, sometimes resulting in different topological states. The contribution of intrinsic SOC to the Hamiltonian can be described by the terms $H_{SO} = i\sum_{\langle i,j\rangle\sigma} \lambda_{ij} \hat{\mathbf{d}}_{ij} \cdot \boldsymbol{\sigma}_{\alpha\beta} \hat{c}^{+}_{i\alpha} \hat{c}_{j\beta}$, where λ_{ij} represents the amplitude of spin–orbit coupling, $\hat{\mathbf{d}}_{ij}$ is the unit vector depending on the type of SOC and $\boldsymbol{\sigma}$ is the vector of Pauli spin matrices. In the ideal kagome lattice, the inclusion of even a small SOC (intrinsic or Rashba SOC) opens a gap around the Dirac point at the K point (resulting in massive Dirac fermions) and separates the flat band from the quadratic bands where the flat band becomes weakly dispersive[46–48] (Fig. 1e). In the time-reversal invariant case, the gap opening leads to non-trivial topological insulating states with $\mathbb{Z}_2$ topology and a robust edge state, giving rise to the quantum spin Hall effect[46]. This situation is distinct from graphene, with its honeycomb lattice, where the Rashba SOC instead hinders the non-trivial phase.

When time-reversal symmetry is intrinsically broken in kagome systems with ferromagnetic order and SOC, the gap opening around the Dirac band and flat band gives rise to non-trivial topological states with non-zero Chern number and dissipationless chiral edge states, which have been detected in the AM_6X_6 compounds (such as $TbMn_6Sn_6$)[37]. In this case, the intrinsic quantum anomalous Hall effect might be realized near the filling of largely gapped Dirac bands[49], resembling the Haldane model in the honeycomb lattice. Partial filling of the flat band (such as 1/3- or 1/2-filled) can give rise to a high-temperature fractional quantum Hall state[50].

Beside SOC, the non-trivial insulating phases can also be driven by a repulsive electronic interaction near the Dirac point and the quadratic band crossing (at the Γ point, where a flat band crosses a quadratic band) as a result of spontaneous symmetry breaking[51–55]. For example, a $\mathbb{Z}_2$ topological insulating state can exist in the kagome system even with negligible intrinsic SOC[53]. For this case, an interaction-driven quantum anomalous Hall effect was proposed around the quadratic band

crossing based on the formation of loop currents on the kagome lattice which spontaneously break time-reversal symmetry and acts analogously to an effective magnetic field or SOC[54]. In addition, the time-reversal symmetry breaking (TRSB) in the kagome lattice can also arise from staggered magnetic flux due to strong SOC that is comparable with the hopping energy[49], and strong on-site repulsion interaction could induce magnetic orders breaking time-reversal symmetry[56–58].

Another important factor for influencing band topology is distortion away from the ideal kagome lattice via spatial symmetry breaking. The breathing kagome lattice is one symmetry-breaking distortion of the ideal lattice that is now being investigated. In this distortion, the bond length and associated hopping amplitude in the adjacent up and down triangles are different (Fig. 1c), leading to the lattice trimerization that breaks inversion symmetry[47,59]. A direct consequence of lattice trimerization is the bandgap opening at the Dirac crossing of the ideal lattice (Fig. 1e). Unlike the effect of SOC, the induced insulating state near the Dirac band in this case is topologically trivial, and the trimerization does not separate the flat band from the other quadratic band at the Γ point. A similar effect arises from dimerization (where two atoms or molecular units form a strong bond resulting a lattice distortion caused by them moving closer together) of the kagome lattice that breaks inversion symmetry.

On including SOC, electronic interaction or orbital degrees of freedom into the breathing kagome lattice or dimerized lattice, various topological states can be induced, including a $\mathbb{Z}_2$ topological insulator and non-trivial Chern phase near the Dirac band and flat band[46,47,60]. In addition, higher-order boundary states have been predicted to appear in a breathing kagome lattice[60–64], where boundary states appear in $d-n$ ($n>1$) dimensions, instead of $d-1$ dimensions as in normal d-dimensional topological insulators. For example, corner states in a 2D artificial breathing kagome lattice have been detected in acoustic systems and photonic waveguides among others[65–67]. Moreover, comparing with the ideal kagome lattice (isotropic), the breathing anisotropy is proposed to be helpful for stabilizing a quantum spin liquid state, such as in $[NH_4]_2[C_7H_{14}N][V_7O_6F_{18}]$ and $Li_2In_{1-x}Sc_xMo_3O_8$ materials[68,69].

Table 1 | Properties of kagome materials

Material	Low-temperature magnetism	Topological features	Electron correlation	Phase transitions
AV_3Sb_5 (A=Cs, K, Rb)	No long-range order but TRSB reported[130,175,176]	Dirac semimetal[34,101]	Weak e–e correlation[136], vHS[101,107], flat band[110]	Structure distortion[138,139], CDW[116], PDW[31], nematic/stripe orders[30,120], superconducting[32]
RMn_6Sn_6	Ferrimagnetic: R=Tb, Dy, Ho, Er (conical magnetic order in R=Dy, Ho)[246] Antiferromagnetic: R=Tm (ref. 246) Antiferromagnetic, double flat-spiral: R=Y, Sc, Lu, Er (refs. 249–251) Ferromagnetic: R=Li, Mg, Ca (refs. 77,256)	Chern phase: R=Tb (ref. 37), Gd–Er (ref. 263), proposed for R=Y (ref. 99) Dirac cone in YMn_6Sn_6 (ref. 99)	Flat band and vHS reported in YMn_6Sn_6 (ref. 99)	Magnetic transitions
RMn_6Ge_6	Ferromagnetic: R=Nd, Sm (ref. 240) Antiferromagnetic: R=Dy–Yb, Sc, Y, Lu, Gd (refs. 238,253)	Not reported	Not clear	Magnetic transition
RFe_6Sn_6,RFe_6Ge_6 (R=Dy–Yb, Sc, Y, Lu)	Mostly antiferromagnetic[238,239]	Not reported	Not clear	Magnetic transitions
RV_6Sn_6	Non-magnetic: R=Y (ref. 257) Weak paramagnetic: R=Sc (ref. 258) Weak, field-dependent magnetism: R=Gd (ref. 257)	Dirac cone in R=Gd, Ho (refs. 262,263)	vHS in R=Gd, Ho (refs. 262,263)	Structural and CDW transitions in ScV_6Sn_6 (ref. 258) Magnetic transition in GdV_6Sn_6 (ref. 257)
$MoCo_6Ge_6$ $Yb_{0.5}Co_3Ge_3$	Paramagnet[259] Weak magnetism, possible magnetic transition around 20 K (refs. 260,261)	Not reported Not reported	Not clear Not clear	Structural transition[259] Structural transition[261]
Nb_3X_8 (X=Cl, Br, I)	X=Cl, Br, paramagnetic to non-magnetic transition (bulk crystal)[39] Thin film: not clear	Not reported	Strong correlation Flat band[42,294,300] Mott insulator[41,42]	Structural and magnetic transition
FeGe FeSn CoSn	Antiferromagnetic[302] Antiferromagnetic[15] Paramagnetic[16]	Not reported Dirac cone[15] Dirac cone[16]	vHS[302] Flat band[15] Flat band[16,17]	FeGe (ref. 302): structural, CDW and magnetic transitions
Mn_3Ge,Mn_3Sn	Chiral antiferromagnetic[20,22]	Weyl semimetal[21]	Not clear	Magnetic transition
$Co_3Sn_2S_2$	Ferromagnetic[14]	Weyl semimetal[13,14]	Flat band[98]	Magnetic transition
Fe_3Sn_2	Non-collinear ferromagnetic, skyrmion[18,19]	Massive Dirac point[310]	Flat band[311]	Magnetic transition
RT_3X_2	Mostly weak magnetism[283–285,308,312,313]	Dirac cone proposed[284,309]	Flat band, vHS proposed[284,309]	Superconducting in compounds such as $LaRu_3Si_2$ (refs. 283,314), $LaIr_3Ga_2$ (ref. 284), YRu_3Si_2 (ref. 285), $LaRh_3B_2$ (ref. 313), $CeRh_3B_2$ (ref. 313)

TRSB, time-reversal symmetry breaking; e, electron; vHS, von Hove singularity; CDW, charge density wave; PDW, pair density wave.

Based on the Dirac states in the kagome lattice, the breaking of inversion (P) or time-reversal symmetry (T) or the combined PT symmetry can split the Dirac point into two Weyl points with opposite chirality, where the surface states of a Weyl semimetal are Fermi arcs connecting two Weyl points. Weyl semimetals that break inversion symmetry were studied extensively in non-magnetic compounds such as the TaAs family and WTe_2. In kagome compounds, the TRSB Weyl semimetal was observed in the ferromagnetic kagome metal $Co_3Sn_2S_2$ (refs. 13,14) and non-collinear antiferromagnetic Mn_3X (X = Sn, Ge)[21,70]. These Weyl states can lead to a chiral anomaly effect, nonlocal transport and Weyl orbit transport[71]. In addition, owing to the large Berry curvature around the Dirac or Weyl bands, kagome materials can have a large intrinsic spin Hall effect[72] and anomalous Hall effect; the latter has been widely observed in TRSB kagome magnets (such as $Co_3Sn_2S_2$, Mn_3X and many AM_6X_6 compounds)[22,73–77]. Owing to the lattice frustration, the kagome lattice is also favourable for inducing topologically non-trivial spin structures in real space, such as skyrmion and scalar spin chirality from non-collinear and non-coplanar spins in kagome magnets, which can give rise to real-space Berry curvature and contribute to a topological Hall effect[78,79]. This effect has been observed in several kagome materials, such as Mn_3Sn (refs. 80,81), Fe_3Sn_2 (ref. 82), Mn_4Ga_2Sn with skyrmions[83] and several AM_6X_6 compounds (such as YMn_6Sn_6, $TmMn_6Sn_6$) with spiral spin structures[84,85].

Flat band and strongly correlated states

The presence of a flat band with highly quenched kinetic energy and a divergence of DOS in a material make it a platform for investigating many-body physics, and partially filling that flat band can lead to exotic strong-electron-interaction-driven quantum states. As discussed above, the effects of SOC and electron interactions can influence the flatness of the flat band and its connection with other bands. Based on these effects, the flat band, and tuning its filling in the kagome lattice, can generate many non-trivial topological states[50,86–89], as well as symmetry-breaking quantum states, including charge or spin orders, nematic phases[51,53,54], ferromagnetism with spin-polarized bands[56,57,90], and Wigner crystallization (a solid phase of electrons)[90–92]. Additionally, a Mott-insulating state can appear in the half-filled flat band, where the electronic band splits into upper and lower Hubbard bands under the effect of strong correlation[42,93]. Doping of the Mott-insulating state is proposed as a possible method for driving unconventional superconductivity[8,94–97], and the frustrated Mott-insulating system is proposed to induce a quantum spin liquid state, where long-range spin exchange can suppress magnetic order[93].

Many physical phenomena arising from flat band physics have been observed in twisted graphene systems. Recently, flat bands have been observed in many kagome materials, including topological metals such as CoSn (refs. 16,17), $Co_3Sn_2Sn_2$ (ref. 98), many AM_6X_6 compounds (such as YCr_6Ge_6 and YMn_6Sn_6)[99,100], and breathing kagome insulators like the Nb_3X_8 family. The Nb_3X_8 family is proposed to be a nearly ideal Mott insulator, with band splitting at the half-filled flat band on the order of 1 eV, and a possible quantum spin liquid (discussed in detail below)[42,93]. These flat-band kagome materials provide a platform for exploring strong-correlation-driven quantum phenomena.

vHSs and related correlation states

Adding to the discussion of correlation in the kagome materials, vHSs contribute to generating Fermi liquid instabilities that can also drive various quantum phenomena. In the kagome lattice, a large DOS at the vHSs strongly enhances the electron correlations. Also, the large DOS combined with a hexagonal Fermi surface near the vHS filling is favourable for inducing strong Fermi surface nesting (in which parallel Fermi surface sheets with same energy of states can be connected by three nesting vectors **Q**) (Fig. 1b), which can create a diverging electronic susceptibility. The Fermi surface nesting and electron correlations can give rise to strong Fermi surface instability. In ideal kagome bands, the vHSs at energy of 0 and $-2t$ have different characters, which belong to a p-type vHS (from the pure sublattice at the M point) and an m-type VHS (mixing of sublattice at M point), respectively (Fig. 1b). One special feature is that the Fermi surfaces at these vHS fillings have inhomogeneous sublattice occupation. For example, at the p-type vHS filling, the Bloch state for the end point of the Fermi surface (M point) is made up by a pure sublattice (one of three sublattices), whereas the Fermi surface has mixed sublattice character between these points, and the nesting vectors connect points on Fermi surfaces dominated by different sublattice occupation (Fig. 1b). The inhomogeneous sublattice occupation and twofold vHS are different from the honeycomb lattice model (two sublattice sites in the unit cell), where the sublattice contribution is homogeneous along the Fermi surface at the vHS filling, and two vHSs at different energy are theoretically identical[44]. The inhomogeneous sublattice contribution can lead to sublattice interference, which weakens the nesting effect of the on-site interaction and affects the emergence of Fermi surface instability[44]. The twofold vHS has been detected in the AV_3Sb_5 family[101] and ScV_6Sn_6 (ref. 102).

Owing to the strong instability near the vHS, the electronic states are unstable against infinitesimal interaction. When the local Hubbard interaction (U_0) and nearest-neighbour site interaction (U_1) are included in the Hubbard model of the kagome lattice, a variety of electronic phases have been proposed in theoretical studies, depending on the relative correlation strength of the included interactions compared with the hopping energy. The appearance of these ordered states is complex and is also influenced by the filling around vHS. The effect from the vHS near $E = 0$ is widely studied, as it is proposed to have a stronger electron-correlation effect than the one at $E = -2t$. Many studies near the $E = 0$ vHS filling indicate that correlations dominated by a very strong U_0 ($U_1 = 0$ or very small) tend to favour magnetism (such as ferromagnetic or antiferromagnetic order) with strong spin fluctuations and chiral spin order[43,103], whereas CDWs, nematic orders and s-wave superconductivity are favoured by long-range correlations from a large U_1 (where U_0 is zero or relatively small). The combined effect of U_0 and U_1 can generate complex states such as spin or charge bond order and unconventional superconductivity[43–45,103]. Tuning the Fermi surface around vHSs influences the different phases based on modulation of the Fermi surface nesting and their correlation strength[45]. Owing to these complex interaction effects around the vHSs, intertwined ordered states can appear, which has happened in AV_3Sb_5.

Note that vHSs with logarithmic divergence of DOS in the kagome lattice are conventional vHSs that have been widely studied; more recent studies proposed a new type of higher-order vHS with power-law divergence of the energy–momentum dispersion relation. Compared with conventional vHSs, the higher-order vHS has imperfect nesting, but flatter band dispersion with substantially enhanced DOS that promises stronger electron correlation and contribution to competing orders[104]. Higher-order vHSs have been studied in twisted graphene[104–106] and also detected in kagome materials like the AV_3Sb_5 family[101,107].

Differences in kagome band structures

Although the kagome lattice theoretically hosts the band-structure properties discussed above, in real materials their presence can vary

considerably. From a chemical view, the electronic properties of real kagome materials are influenced by several factors, such as the orbital composition, bonding of the elements in kagome lattice, the interaction between the kagome lattice and neighbouring out-of-plane sublattices, the orbital filling, and the electronegativity of elements[108,109]. By analysing the geometrical and band properties of more than 3,000 compounds featuring kagome lattices, it was shown that some simple chemical rules can be used for predicting the kagome band property[108]. Strong interlayer interaction tends to destroy the kagome band features in materials with linked kagome lattices, where the kagome net and the nearest out-of-plane sublattice have the same or similar kinds of atoms (for instance, of the same group), and the bond length between the kagome atoms (d_K) is equal or similar to the bond length to their out-of-plane neighbour atoms (d_{NN}). Clean kagome bands near the Fermi level typically appear in materials with isolated kagome lattices ($d_K/d_{NN} \leq 1.1$), such as CoSn, FeSn, AV_3Sb_5 and AM_6X_6 compounds, and in semi-interacting kagome lattices ($1.1 \leq d_K/d_{NN} \leq 1.4$) such as $Co_3Sn_2S_2$. In these systems, partially filled atomic orbitals of the atoms comprising the kagome lattice are necessary to form bonds between the kagome atoms and induce clean kagome bands near the Fermi level. If the orbital is fully filled, the kagome bands tend to lie below the Fermi level, and more dispersive bands arising from the interlayer bonding dominate the electronic properties. In compounds with strongly interacting lattices ($d_K/d_{NN} \geq 1.4$), the typical kagome bands can be lost, for example in materials with kagome lattices formed from a transition metal surrounded by electronegative non-metals such as Cl, N or O (the *d* electrons in a kagome lattice become localized on the atomic sites). However, the kagome bands can exist in some compounds with kagome lattices formed by Cu, Ag or Au atoms (such as herbertsmithite or $ZnCu_3(OH)_6Cl_{12}$).

Intertwining of phases in the topological kagome metal AV_3Sb_5

AV_3Sb_5 (A = K, Cs, Rb) is a representative kagome family that presents electronic phases, including a cascade of varying charge orders and a superconducting state with decreasing temperature. In this section, we discuss the studies of the origin of these states, their symmetry breaking, intertwining and competition with superconductivity (including its nature).

Crystalline and electronic band structures

The family members of AV_3Sb_5 crystallize in the hexagonal structure space group *P6/mmm* (preserving inversion symmetry) and have an A–Sb2–VSb1–Sb2–A stacking order[26]. The 2D kagome lattice of V atoms is in the VSb1 layer, with Sb1 atoms filling in the hexagonal centres (Fig. 2a). The honeycomb lattices of Sb2 atoms are located above and below the triangle centres of the kagome lattice, and the Sb2–VSb1–Sb2 sublattice is separated by the alkali atoms. Owing to the weak bonds between the alkali atom and the Sb layer, the AV_3Sb_5 family is readily cleaved between the alkali layer and the Sb layer; the cleaved Sb surface is more stable than the alkali surface where the alkali ions easily migrate[30].

In momentum space, the AV_3Sb_5 family presents a quasi-2D Fermi surface around the centre (Γ point) of the Brillouin zone, generated primarily by its Sb p_z orbitals, consistent with the strong anisotropy of the layered structure (Fig. 2b,c). The normal state of the AV_3Sb_5 compounds is calculated to be a Z_2 topological metal, and the vanadium kagome net contributes to the appearance of multiple Dirac points at K and H points (Fig. 2d), with gaps opening under the influence of SOC, and topological surface states appearing at the $\overline{M}$ point near the Fermi level[101,110,111]. In addition, two kinds of vHSs with saddle-point behaviour arising from the V *3d* orbital at the M point have been observed through high-resolution angle-resolved photoemission spectroscopy (ARPES) (CsV_3Sb_5; refs. 101,107). One is an m-type vHS with a mixed sublattice and perfect Fermi surface nesting, the other is p-type vHS with a single sublattice. These two vHSs at each Fermi surface possess opposite concavity, and the Fermi surface can have opposite fermiology (electron-like or hole-like). Besides the conventional vHS with quadratic energy–momentum dispersion, a p-type vHS (vHS1) near the Fermi level is found to be a higher-order vHS with energy–momentum dispersion close to a quartic polynomial along one direction, which has less-pronounced Fermi surface nesting. In addition, a flat band runs across the entire momentum space below the Fermi level ($E \approx -1.2$ eV) alongside another non-dispersive feature near the Fermi level in CsV_3Sb_5, indicating electron correlations induced by the kagome lattice[110].

CDWs and symmetry breaking

Members of the AV_3Sb_5 family behave like good metals with rich phase transitions when decreasing temperature. A first phase transition can be seen between 78 K and 103 K (Fig. 3c) and has been observed for all family members via resistivity, magnetization and heat-capacity measurements[26,32,33,112]. This transition has been found to be an onset of CDW order of first-order type[113–115]. Below T_{CDW}, scanning tunnelling microscopy (STM) studies, which are surface-sensitive, revealed an in-plane $2a_0 \times 2a_0$ superstructure (wavevector of $\mathbf{Q}_{3q\text{-}2a} = 1/2\mathbf{Q}_{Bragg}$) along all three directions of the kagome lattice on both the Sb and alkali surfaces[30,31,116–120]. Besides the $2a_0 \times 2a_0$ CDW structure, a unidirectional $4a_0$ stripe CDW order ($\mathbf{Q}_{1q\text{-}4a} = 1/4\mathbf{Q}_{Bragg}$) is observed in some of the STM studies of CsV_3Sb_5 (Fig. 3b) and Sn-doped CsV_3Sb_5 on the Sb surface below 40–50 K (refs. 30,121,122), as well as on Sb-terminated RbV_3Sb_5 (refs. 118,123). It becomes weak with more surrounding Cs atoms on the Sb surface[124] and was not observed on the Cs surface[120], nor in KV_3Sb_5 (refs. 116,117). A unidirectional $\sqrt{3}a_0$ in-plane charge order is also observed in RbV_3Sb_5 by STM, which is sensitive to the surface Rb atoms desorption, implying a sensitivity to A-site stoichiometry[123]. The $4a_0$ CDW unidirectional order has not been detected in bulk measurements, such as X-ray diffraction or nuclear magnetic resonance (NMR). The origin of the $4a_0$ CDW order is proposed to be a surface state that may be sensitive to the Fermi surface and chemical potential[119]. Based on microfocused ARPES, a polar nature of the differently terminated surfaces has been revealed in AV_3Sb_5, where the surface of the A-termination is electron-like and the Sb-termination is hole-like[125,126]. Additionally, the A-terminated surface shows band folding from the bulk CDW phase, which was not evident on the Sb-terminated surface, owing to the polar charge. The suppression of bulk CDW order on the Sb-termination might be related to the appearance of unidirectional order. In addition, a combined STM–ARPES study reported the reconstruction of small hole pockets in the Fermi surface (part of bulk bands generated by the CDW order) when stripe order appears, indicating that the generation of stripe order might also be related to the bulk CDW bands[127]. The in-plane phonon instability and out-of-plane interaction are also proposed to play important roles in the formation of $4a_0$ CDW order[128]. However, the definitive origin of the unidirectional order and why it varies in the different materials and surfaces remain important open questions.

Besides the unidirectional charge orders breaking rotation symmetry, the C_2 symmetry of the electronic state observed in early STM studies of the Cs surface is found to originate from an electron-driven bulk nematic phase transition with $T_{nem} \approx 35$ K, demonstrated by NMR measurement and elastoresistance measurements[120].

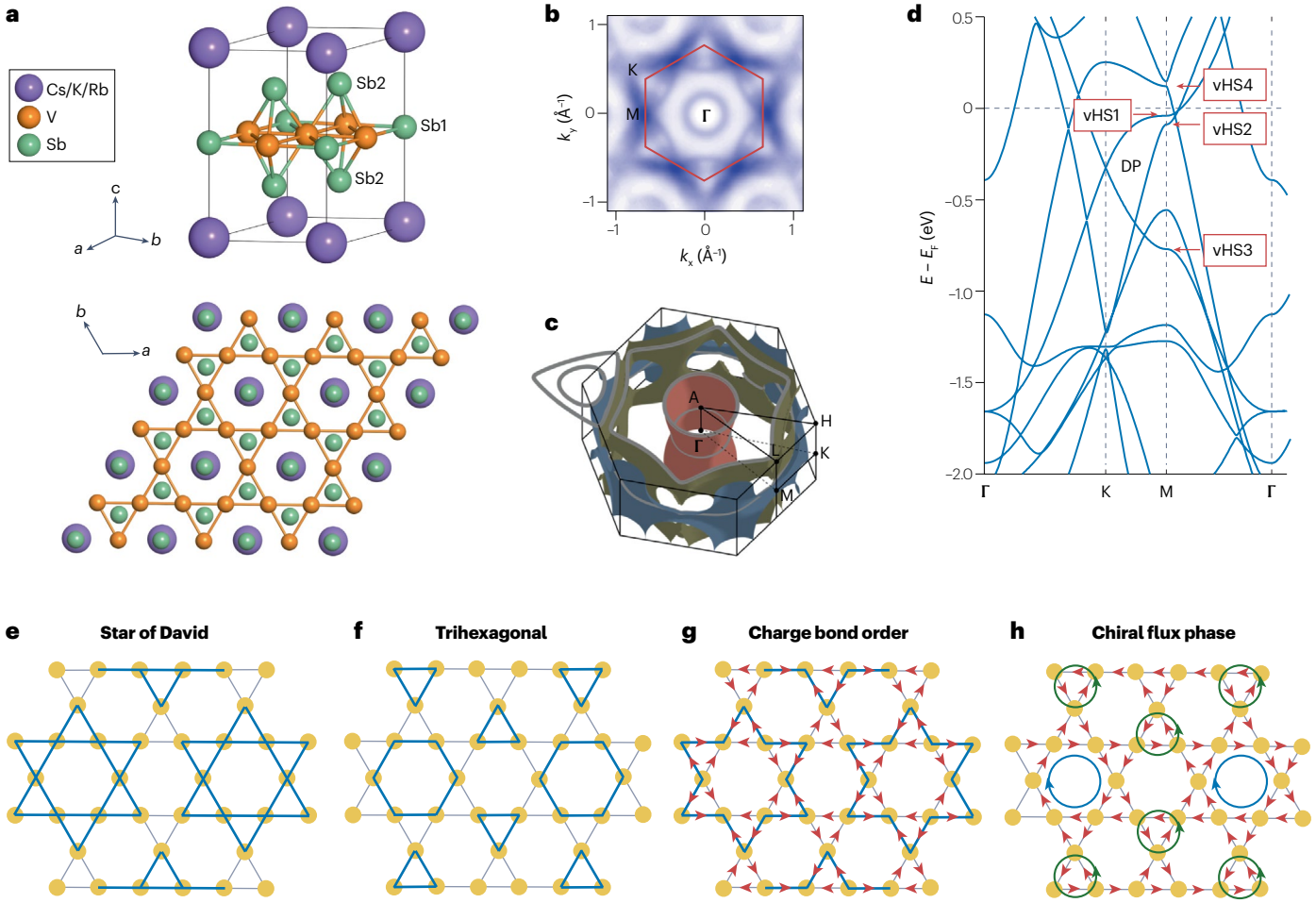

Fig. 2 | Lattice structure and electronic band structure of AV_3Sb_5. **a**, Basic structure of AV_3Sb_5 (A = Cs, K, Rb). **b**, Fermi surface of KV_3Sb_5, measured by high-resolution angle-resolved photoemission spectroscopy (ARPES). **c**, Fermi surfaces for undistorted CsV_3Sb_5 in the hexagonal Brillouin zone. **d**, Band structure of CsV_3Sb_5. E_F, Fermi energy; vHS, van Hove singularity; DP, Dirac point. **e**–**h**, Possible charge-order states predicted for AV_3Sb_5 family: Star of David structure (part **e**), trihexagonal structure (part **f**); one kind of predicted charge bond order that breaks time-reversal symmetry (TRS) (part **g**); and one kind of chiral flux phase that breaks TRS (part **h**). Part **b** adapted with permission from ref. 34, AAAS. Part **c** adapted with permission from ref. 139 under a Creative Commons licence CC BY 4.0. Part **d** adapted with permission from ref. 107 under a Creative Commons licence CC BY 4.0.

Coherent quasiparticles with unidirectional electronic scattering are also observed below 30 K without observation of $4a_0$ order[121]. Although the stripe-like $4a_0$ CDW order (smectic order) and nematic orders are reported in different studies, the rotation symmetry breaking from C_6 to C_2 symmetry is definitively observed in the $2a_0 \times 2a_0$ CDW structure for all the family members. Differential conductance measurements from STM show that the energy modulation of the $2a_0 \times 2a_0$ CDW intensity along one direction is different from that of the other two directions at low temperature, thereby breaking C_6 rotational symmetry[30,117,119,120]. Many following studies reported that the rotation symmetry breaking and nematicity from the structural distortion of the 3D CDW order starts just below T_{CDW} (refs. 115,120,121,129–133). In addition, three nematic domains oriented at 120° to each other have been detected below T_{CDW} (ref. 130) (Fig. 3i). The C_2 structural distortion is proposed to arise from a π-phase shift of the CDWs between two adjacent kagome layers[120,124,129,130,132,134,135]. The 3D CDW phase with $2 \times 2 \times 2$ superlattice is widely detected in this family[115,124,136–138]. However, the $2 \times 2 \times 4$ order at low temperature[139,140], the $2 \times 2 \times 1$ (ref. 141), and the coexistence of $2 \times 2 \times 4$ and $2 \times 2 \times 2$ CDW stacking phases[142], and transition from the $2 \times 2 \times 4$ (between 60 K and T_{CDW}) to the $2 \times 2 \times 2$ orders (below 60 K)[138] are also reported in CsV_3Sb_5 via X-ray diffraction measurement. The appearance of different orders is sensitive to temperature[123,138,142,143], pressure[141], surface construction, synthesis and other factors, implying that they might be close in energy and metastable under certain conditions[138,144].

The mechanisms for the formation of the various charge orders are complex in the AV_3Sb_5 family. In general, the CDW order originates from weak coupling based on Fermi surface instabilities related to nesting[145], and also from strong coupling based on electron–phonon or electron–electron interaction[146]. For AV_3Sb_5, high-resolution ARPES measurements have shown 3D CDW-induced Fermi surface reconstruction and associated band splitting below T_{CDW} (refs. 147,148). Both the m-type vHS with strong Fermi surface nesting and the higher-order p-type vHSs near the Fermi level are observed to open a gap in CsV_3Sb_5

(refs. 101,111,149,150), and the gap openings of the vHSs are observed in the original and reconstructed Fermi surfaces, as well as in KV_3Sb_5 and RbV_3Sb_5 (refs. 147,151). The CDW order is also found to be related to inter-saddle-point scattering around different vHSs[152]. These results suggest the importance of Fermi surface nesting for the formation of CDW order[101,111,147,149,150], which is also supported by optical spectroscopy studies[153,154]. In addition, the results of hard X-ray scattering experiments with (Cs, Rb)V_3Sb_5 indicate the absence of soft phonon modes, suggesting weak electron–phonon coupling[136]. Conversely, the Raman scattering measurement of CsV_3Sb_5 detected amplitude modes with large frequencies and strong hybridization with other lattice modes, suggesting a strong electron–phonon coupling CDW, although soft phonons are absent[155]. It was proposed that the CDW transition in the AV_3Sb_5 family is a weak first-order CDW transition without continuous change of lattice dynamics, which might be related to the absence of phonon softening[134,136]. The important role of electron–phonon interactions in the CDW state is also reported in ARPES[156] and optical studies[157] of KV_3Sb_5 as well as neutron scattering experiments in CsV_3Sb_5[158]. Moreover, density functional theory calculations show unstable phonon modes at both M and L points of the hexagonal Brillouin zone, and the condensation of these phonon modes is proposed to drive the formation of the CDW[128,137,159,160]. Combining these results, both electron–phonon coupling and Fermi surface nesting should play important roles in the formation of CDW states.

Different ground-state structures of the CDW state have been proposed in theory[135,161–164], but the exact CDW structure is still under debate, owing to the complex charge orders and symmetry breaking. Based on an in-plane 2×2 CDW distortion without rotation breaking and TRS, the Star of David (SoD) and trihexagonal (TrH) breathing distortion (also called inverse Star of David in many publications) are candidates for the CDW phases[160], where V atoms either move away from or closer to Sb1, respectively (Fig. 2e,f). As discussed above, the CDW order is 3D with rotation symmetry breaking which is induced by a phase shift between adjacent layers. For these two structures, the TrH structure is found to be favoured, with lower energy in many theoretical investigations[134,137,160]. The nuclear magnetic resonance results in CsV_3Sb_5 (ref. 165) and RbV_3Sb_5 (ref. 166) and in associated theoretical study[167] reported the staggered TrH ordering with interlayer π-shift of the CDW phase. The ARPES study also reported staggered TrH structures with interlayer shifts for KV_3Sb_5, RbV_3Sb_5 and Sn-doped CsV_3Sb_5 (ref. 147); however, alternating SoD and TrH orders were reported to be the favoured structures in CsV_3Sb_5 (refs. 147,168). The large number of quantum oscillation frequencies found in the transport study of CsV_3Sb_5 also suggests a complex structural distortion that cannot be explained with only SoD or TrH order, implying interlayer ordering[169]. Compared with KV_3Sb_5 and RbV_3Sb_5, which normally possess $2 \times 2 \times 2$ order with staggered TrH order, CsV_3Sb_5 seems to have a more complex CDW state, where $2 \times 2 \times 2$ CDW, $2 \times 2 \times 4$ CDW and coexistence of these orders are reported in many X-ray studies[138–140,142,170], as well as a transition from $2 \times 2 \times 4$ CDW order to $2 \times 2 \times 2$ in $CsV_3Sb_{5-x}Sn_x$ under light Sn substitution[170]. The different stacking in distinct compounds may be related to the increased instability of the TrH state when the A site changes from K to Rb to Cs (ref. 140), and the complex 3D CDW states in CsV_3Sb_5 may be formed from the combination of SoD and TrH orders[140,142,147,168]. In addition, an ARPES study suggests that the superconducting phase diagram under Sn doping shows correlation with the CDW phase[147]. For example, T_c is close to the maximum when the CDW changes from alternating SOD and TrH order stacking to the staggered TrH structure in $CsV_3Sb_{5-x}Sn_x$. This result also implies that the charge-order structure is closely related to superconductivity here. Further work to elucidate the link between the order stacking and superconductivity is needed.

Besides rotation symmetry breaking, TRSB below the CDW transition is one crucial question that is discussed for AV_3Sb_5. So far, no long-range magnetic order has been observed in the AV_3Sb_5 family[26]. The absence of local magnetic moments was reported in an early muon spin spectroscopy (μSR) of KV_3Sb_5[171], and a similar result was reported in STM studies of CsV_3Sb_5 and KV_3Sb_5 with the CDW order showing no magnetic field dependence[117,172], and a polar optical Kerr measurement suggesting no Kerr signal from TRSB in CsV_3Sb_5 (ref. 173). However, many studies show a signal of TRSB below the CDW transition. A chiral CDW order was detected in several STM studies[116,118,119] (Fig. 3e), and a clear signal of local magnetic field appearing below the CDW transition was observed in a recent zero-field μSR measurement[174–176] (Fig. 3f), indicating TRSB. The μSR experiment also shows an anisotropic internal field with local field direction changing from the *ab* plane to the *c* axis below ~30 K (ref. 176), consistent with the $4a_0$ or nematic order transition temperature. Additionally, electrical transport measurements detected a giant anomalous Hall effect dominated by an enhanced skew scattering effect[34,35,74], and a large anomalous thermal Hall and Nernst effect in the CDW state of AV_3Sb_5 (refs. 177–179), consistent with TRSB. Signals of the zero-field Kerr effect and circular dichroism are detected concomitant with the CDW transition[130,131,180], and nematic domains (of size ~100 μm) with opposite signs are detected without applying external magnetic field[130,180]; the domains are magnetic-field-tunable[180]. These results provide further strong support of spontaneous TRSB.

Theoretically, the TRSB chiral flux phase[181] and charge bond order[162,182] with orbital currents are proposed by including nearest-neighbour (U_1) interactions based on the unique sublattice structures of the kagome lattice. Examples of these orders are shown in Fig. 2g,h. The chiral flux phase with orbital loop current is proposed to be the favoured state for TRSB[162], where the opposite chiral fluxes generated by the loop currents for the hexagons and triangles in the kagome lattice induce an uncompensated net flux in the unit cell. The long-range next-nearest-neighbour Coulomb repulsion is also proposed to help stabilize the loop current[183]. The loop current structure may explain many experimental observations, such as the appearance of local magnetization and non-zero Kerr signals[130,174,176,180]. In particular, although the AV_3Sb_5 family seems centrosymmetric, the second-harmonic Hall measurement shows signs of magnetochiral anisotropy for in-plane magnetic field below ~35 K (ref. 184), and the chirality is switchable by a small out-of-plane field component that can be attributed to the chiral CDW phase with orbital loop current (Fig. 3h). The existence of TRSB order suggests that long-range electron–electron interactions in AV_3Sb_5 should also contribute to the formation of charge orders. In addition, it is proposed that owing to the twofold vHS in AV_3Sb_5, with distinct electron-like and hole-like Fermi surface properties, a chiral exciton can appear based on electron–hole pairs and lead to chiral excitonic order, which can be another source for TRSB[185].

Superconductivity and pairing mechanism

Cooling further to very low temperatures, superconductivity appears in the AV_3Sb_5 compounds (Fig. 3a) with $T_c \approx 2.5$ K in CsV_3Sb_5 and $T_c \approx 0.92$–0.93 K in KV_3Sb_5 and RbV_3Sb_5 at ambient pressure[32,33,112]. The $2a_0 \times 2a_0$ CDW phase with rotation symmetry breaking and either a $4a_0$ CDW or nematic phase are also observed to persist into the superconducting state, indicating smectic or nematic superconductivity[30,31,120,129] with

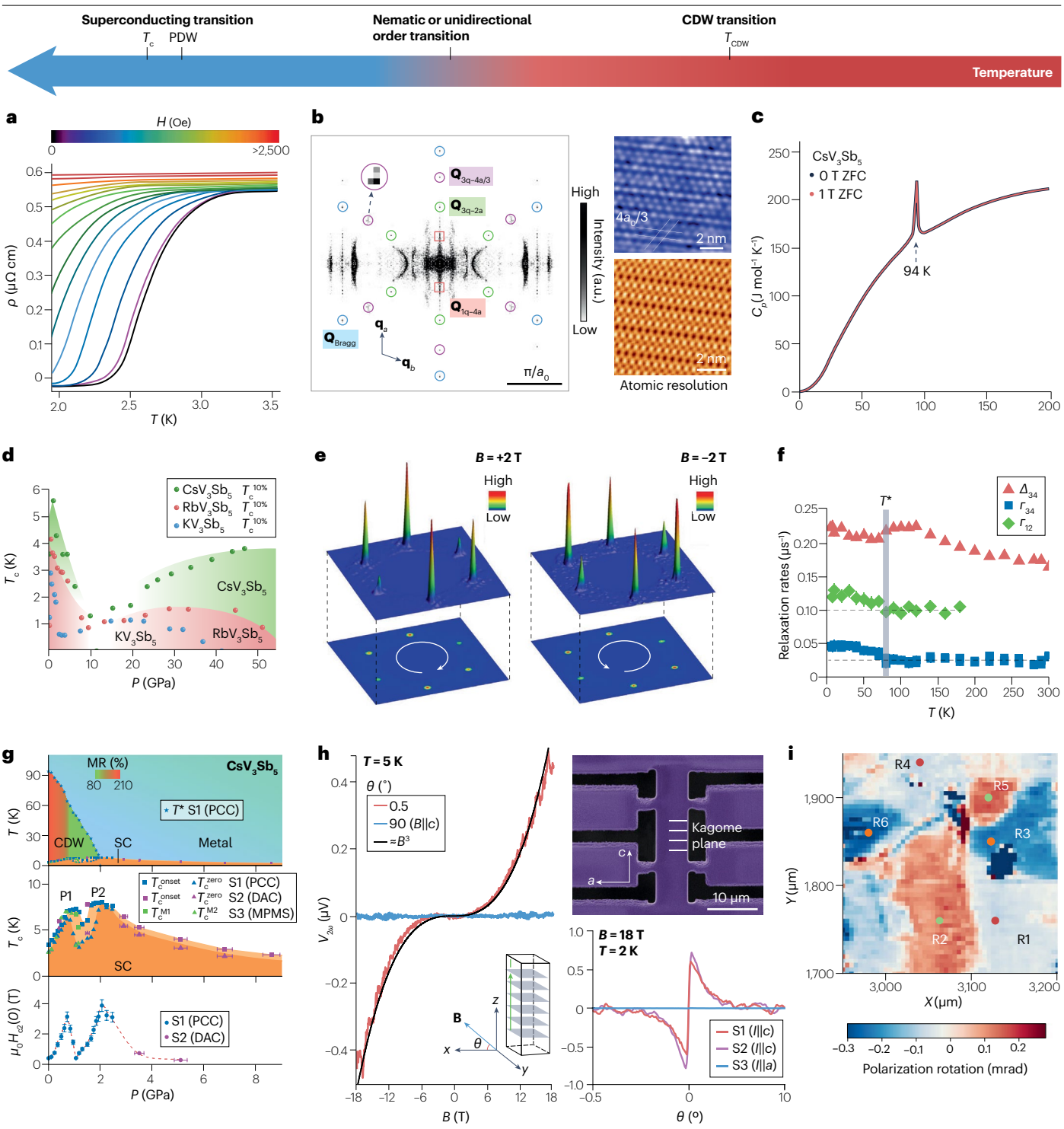

twofold symmetry. In addition to these phases, a PDW ($\mathbf{Q}_{3q\text{-}4/3a} = 3/4\mathbf{Q}_{Bragg}$) phase has been detected via STM study of CsV_3Sb_5 on the Sb surface (Fig. 3b). Distinct from other, long-range, charge orders, the PDW phase is a short-range order[31]. Both CDW and PDW order persist after breaking superconductivity using a high magnetic field or increasing the temperature just above T_c. In addition, the temperature-dependent dI/dV spectrum reveals a pseudogap phase with PDW order observed only in the energy range of the pseudogap, which is unlike the CDW phases that persist at all energies. This special 3D PDW phase is proposed to be the 'mother' phase responsible for the pseudogap, in direct analogy to the cuprate high-temperature superconductors[1,31], where a primary order spontaneously breaks multiple symmetries and the resultant 'daughter' phases with lower symmetries are suggested to be melted versions of the mother phase. The combination of ARPES and STM measurement

Fig. 3 | Representative physical properties of AV_3Sb_5. **a**, Superconductivity at low temperature. T, temperature; ρ, resistivity; H, magnetic field. **b**, $2a_0 \times 2a_0$ charge density wave (CDW) order ($\mathbf{Q}_{3q\text{-}2a} = 1/2\mathbf{Q}_{Bragg}$), $4a_0$ CDW order ($\mathbf{Q}_{1q\text{-}4a} = 1/4\mathbf{Q}_{Bragg}$) and pair density wave (PDW) order ($\mathbf{Q}_{3q\text{-}4/3a} = 3/4\mathbf{Q}_{Bragg}$), measured by scanning tunnelling microscopy (STM) and scanning tunnelling spectroscopy (STS) in CsV_3Sb_5. **Q** represents the wavevector. The left panel is the Fourier transform showing these orders; the top right panel is a $dI/dV(r,V)$ map, exhibiting a $4a_0/3$ chequerboard modulation associated with the PDW order; the bottom right panel is the atomically resolved STM image showing the $\mathbf{Q}_{1q\text{-}4a}$ spatial modulation. **c**, CDW transition measured in CsV_3Sb_5. C_p, heat capacity; ZFC, zero-field cooled. **d**, Superconducting phase diagram under high pressure P. T_c, critical temperature. **e**, Chiral charge order detected by STM in KV_3Sb_5. B, magnetic field. **f**, Signal of time-reversal symmetry breaking measured by high-resolution muon spin scattering in KV_3Sb_5. Δ and Γ are muon spin relaxation rates related to the nuclear and electronic systems, respectively. T^*, charge order transition temperature. **g**, Double-dome superconducting phase diagram under relatively low pressure. DAC, diamond anvil cell; MPMS, magnetic properties measurement system; MR, magnetoresistance; $\mu_0 H_{c2}$, upper critical field; PCC, piston cylinder cell; SC, superconductor; T_c^{onset}, superconducting transition temperature where the resistance starts to drop; T_c^{zero}, superconducting transition temperature where the resistance reaches zero. **h**, Chiral transport with second-harmonic-generation (SHG) signal detected in CsV_3Sb_5. The device is shown at the top right. The right bottom panel is angle dependence of SHG signal, which is switchable by the out-of-plane magnetic field. **i**, Three nematic domains detected in RbV_3Sb_5 by birefringence measurement. The red, white and blue regions show the domains. Part **a** adapted with permission from ref. 32, APS. Part **b** adapted with permission from ref. 31, Springer Nature Ltd. Part **c** adapted with permission from ref. 32, APS. Parts **d** adapted with permission from ref. 218, APS. Part **e** adapted with permission from ref. 116, Springer Nature Ltd. Part **f** adapted with permission from ref. 175, Springer Nature Ltd. Part **g** adapted with permission from ref. 213 under a Creative Commons licence CC BY 4.0. Part **h** adapted with permission from ref. 184, Springer Nature Ltd. Part **i** adapted with permission from ref. 130, Springer Nature Ltd.

shows that the appearance of PDW order is related to a set of small hole pockets in CsV_3Sb_5 that come from the CDW transition[127]. The origin of the PDW is still an open question, needing deeper experimental and theoretical studies.

With diverse CDWs intertwining with superconductivity and multiple superconducting gaps[149,186,187] in the AV_3Sb_5 family, the pairing of the superconducting state and the fundamental question of conventional or unconventional superconductivity has been hotly debated. In general, conventional *s*-wave superconductivity is fully gapped with a nodeless isotropic superconducting gap, which is robust to non-magnetic impurity scattering. Unconventional superconductivity with a sign-changing superconducting order parameter can induce nodes in the superconducting gap[186,188]. In some studies on CsV_3Sb_5, *s*-wave superconductivity with fully gapped or nodeless superconductivity was reported (refs. 113,188), evidenced by the appearance of the Hebel–Slichter coherence peak at ambient pressure in the nuclear quadrupole resonance (NQR) and NMR measurement[113], as well as exponential behaviour of the magnetic penetration depth $\Delta\lambda(T)$ in a tunnelling diode oscillator measurement (which deviates from the linear or power-law temperature dependence for nodal superconductivity)[188]. Although some studies reported sign-preserving superconductivity or s-wave superconductivity in CsV_3Sb_5, the superconducting states possessed features of multiple bands and an anisotropic superconducting gap. For example, two-gap ($s + s$)-wave symmetry was reported via μSR measurement (bulk probe) with a large value of T_c/λ_{ab}^{-2} (λ_{ab} is the in-plane magnetic penetration depth) that is far from conventional superconductivity[187]. And an anisotropic bulk superconducting gap that was detected by measuring magnetic penetration depth, using electron irradiation effects, was speculated to be a new type of unconventional superconductivity due to complex charge orders[189].

In addition, the direct characterization of the superconducting gap using STM shows distinct gap shapes on different surfaces. In general, a U-shaped superconducting gap reflects the fully gapped isotropic gap, and a V-shaped superconducting gap may be related to an anisotropic superconducting gap and possibly unconventional superconductivity. In experiments, a V-shaped gap (possibly related to Fermi surfaces contributing to an anisotropic CDW gap) as well as a U-shaped gap (isotropic and less affected by the CDW) was seen on both the half-Cs and Sb surfaces of CsV_3Sb_5 (ref. 186). Multiple-band sign-preserving or *s*-wave superconductivity is proposed based on the in-gap states that can be induced by magnetic clusters, but not by non-magnetic impurities[186]. The V-shaped gap is also reported on both Cs and Sb surfaces in CsV_3Sb_5 in other STM works[31]. Other STM studies reported unconventional zero-bias conductance peaks in the V-shaped gap of the vortex-core state on the half-Cs surface of CsV_3Sb_5, which may correspond to possible Majorana bound states from topological surface states[124]; this is supported by theory when the contribution of the charge-ordered states is taken into account[190]. The appearance of different types of superconducting gaps on the different surfaces in different studies might be related to modulation of the Fermi surface and charge orders[186,191], which can influence the superconducting properties. As mentioned above, the cleaved surfaces with differing terminations are polar with distinct fermiology related to the CDW states[126]. TRSB charge-ordered states like the chiral flux charge order are also proposed to influence the superconducting properties[192], which would make it possible to change a U-shaped gap to a V-shaped gap[191].

Unconventional superconducting signals with nodal gaps have also been observed in other investigations, including thermal conductivity[193], NQR and μSR experiments. A μSR experiment reported nodal superconductivity in RbV_3Sb_5 and KV_3Sb_5 with magnetic penetration depth showing linear-in-T behaviour at ambient pressure, whereas a transition from nodal to nodeless superconductivity is observed when increasing pressure[194]. The large value of T_c/λ_{ab}^{-2} detected in (K,Rb)V_3Sb_5 also implies unconventional superconducting pairing[175,194]. In addition, early μSR experiments reported TRSB below the CDW transition, but no TRSB in the superconducting state because there is no change of the muon spin relaxation rate during the superconducting transition[187,195]. However, by applying pressure to suppress the signal of the charge order, the zero-field muon spin relaxation rate did show an increase below the superconducting transition in KV_3Sb_5 (1.1 GPa), RbV_3Sb_5 (1.85 GPa) and CsV_3Sb_5, indicating TRSB in the superconducting state and implying an unconventional pairing state[194,196]. NQR experiments reported the absence of the Hebel–Slichter coherent peak when the pressure is above the P_2 of second superconducting dome[197] in CsV_3Sb_5, also suggesting unconventional superconductivity. Superconductivity of the surface states and signals of possible spin-triplet superconductivity were also seen in proximitized $K_{1-x}V_3Sb_5$ Josephson junctions[198].

Theoretically, both *s*-wave and unconventional superconducting pairing are proposed in the AV_3Sb_5 family. It was reported that the electron–phonon coupling is too weak for the superconducting T_c in these materials, suggesting possible unconventional pairing[160]. In this family, the local correlation (on-site) is also proposed to be weak, and non-local electron correlation might be crucial[199]. By including both local correlation and nearest-neighbour Coulomb repulsion, rich pairing symmetries are found near the vHSs with competitive spin-triplet and spin-singlet pairing[200–202]. The favoured pairing state is highly dependent on the non-local Coulomb interaction, interaction strength, Fermi momentum and van Hove bands[200–202]. For instance, a dominant *f*-wave spin-triplet superconducting order is theorized to be favoured for weak coupling, whereas *d*-wave singlet pairing competes with *p*-wave pairing under very strong correlation[200]. The complex electronic bands with multiple vHSs, and the sensitivity of superconductivity to the Fermi surface and electron correlations show the possibility of controlling superconducting pairing in the AV_3Sb_5 family. One study suggests an unusual charge pairing (that is, charge 4e or 6e) beyond the normal charge-2e pairing superconductivity[203–206]. Such charge pairing may happen based on the PDW superconductivity or on the nematic or stripe superconducting state[206,207]. Charge-4e and 6e superconductivity was reported in CsV_3Sb_5 by measuring the magnetic flux quantization during the superconducting transition region, based on the Little–Parks effect[208], where the effective flux area in CsV_3Sb_5 is reported to be determined by the inner ring area. The unusual effective flux area in the Little–Parks measurement[209] and non-uniform vestigial charge-4e phase are also discussed in theory[210]. However, investigation of these unusual charge pairings has only just begun, and it is premature to draw a strong conclusion; more investigations are required to verify the pairing and have a clear understanding of the mechanism.

Intertwining of ordered states

Given the coexistence of superconductivity and CDW order, it is important to understand the relation between them and the underlying mechanism of modulating the states. These were studied by extensive tuning methods including pressure, chemical and electrical doping, layer dependence and strain[211–217]. The superconductivity shows prominent competition with the CDW order, and multiple superconducting domes have been detected in the AV_3Sb_5 family. By applying pressure in a relatively low region ($P < 10$ GPa), a superconducting dome with T_c reaching a maximum around $P_1 \approx 0.5$ GPa was observed in KV_3Sb_5, while two superconducting domes with a shallow valley between them were observed in $(Cs,Rb)V_3Sb_5$, where $P_1 \approx 0.6$–0.7 GPa and $P_2 \approx 2$ GPa for CsV_3Sb_5 (refs. 212,213); $P_1 \approx 1.5$ GPa, $P_2 \approx 2.4$ GPa for RbV_3Sb_5 (ref. 112). The superconductivity is highly suppressed around 10 GPa in these materials. However, superconductivity returns upon applying even higher pressure, and a new superconducting dome is observed with $P_2 \approx 22$ GPa for KV_3Sb_5 (refs. 211,218), $P_3 \approx 28.8$ GPa for RbV_3Sb_5, and $P_3 \approx 53.6$ GPa for CsV_3Sb_5 (refs. 193,218–220) (Fig. 3d). Associated with the superconducting domes, the CDW transition temperature reduces with increasing pressure, and the CDW order is completely suppressed around P_1 of KV_3Sb_5 and P_2 of $(Cs,Rb)V_3Sb_5$ (refs. 112,211–213). The result in CsV_3Sb_5 is shown in Fig. 3g. A new CDW order starts to appear when superconductivity reduces above P_2 in KV_3Sb_5, which may correspond to a distinct CDW state[211]. In addition, NMR experiments suggest that the two domes appearing in CsV_3Sb_5 in the low-pressure region are related to the appearance of a stripe-like CDW order with $4a_0$ modulation between P_1 and P_2 (ref. 197).

So far, no structural phase transition is reported under pressure in these compounds[219,220], and the tuning of the superconductivity and CDW order is proposed to be related to the changing of Fermi surface instability and electron–phonon coupling. Theoretical calculations show that the pressure reduces the c/a ratio, associated with a slight change of the in-plane lattice parameter, but a large enhancement of the out-of-plane parameter due to the Sb bonding and related out-of-plane hopping. As a result, the Fermi surface was found to have a large reconstruction on the Sb p_z band, with only slight changes on the *V* bands. Beside the influence of Fermi surface nesting, the Sb p_z bands are proposed to have a large contribution to the tuning of superconductivity and re-entrance of superconductivity at high pressure[221,222]. Associated with the band reconstruction, the re-entrant superconductivity may be related to the Lifshitz transition and enhanced electron–phonon coupling due to partial phonon softening at high pressure[219,220].

A similar competition between the CDW order and superconductivity is also detected by electrical and chemical doping, such as Cs doping[215], as well as Nb (refs. 214,223) and Ti (ref. 224) substitution of V atoms, and Sn (refs. 225,226) substitution of Sb. The Nb, Ti and Sn substitutions act as hole dopants, which induce strong suppression of the CDW order accompanied by enhancement of superconductivity. Similar hole doping results are also found in oxidized thin CsV_3Sb_5 flakes[227]. Theoretically, the hole doping is highly orbital-selective[222,226,228], and mainly dopes the Γ band (formed by the Sb p_z orbital) and higher-order vHS with weak Fermi surface nesting. ARPES measurements[223] in Nb-doped CsV_3Sb_5 reported that the shift of the vHS reduces the Fermi surface nesting around E_F, leading to reduction of the CDW gap and suppression of the CDW order, whereas the expansion of Sb-derived Γ electron bands and recovery of V-derived density of states are attributed to the enhancement of superconductivity. In addition, electron doping by injecting Cs on the surface of CsV_3Sb_5 is also reported to be highly orbital-selective[215], where the Γ band contributed by the Sb p_z orbital shifts downward and the Fermi surface is expanded after doping, but the CDW gap around the Fermi level is reduced. The competition of CDW order and superconductivity is also realized by reducing the film thickness of CsV_3Sb_5. A maximum of T_c and minimum of T_{CDW} appears around 27 layers, which is attributed to a crossover from electron–phonon coupling to electronic interactions[229]. A metal-to-insulating transition is detected for very thin films (fewer than five layers) or through protonic gate tuning[230], which could modulate the disorder and carrier density for the modulation of superconductivity and CDW order. Monolayer AV_3Sb_5 is proposed to possess a variety of competing instabilities such as doublets of CDW order and *s*-wave and *d*-wave superconductivity[231].

Clear understanding of charge orders and superconducting properties of the AV_3Sb_5 family still requires more effort, especially the elucidation of the charge-ordered ground state, TRSB ordered state, and superconducting pairing, which are critical for future investigations of unconventional superconductivity and topological superconductivity. So far, most studies in AV_3Sb_5 are based on bulk samples; only a few investigations have been on thin samples. Thin films of the AV_3Sb_5 may yield insights on CDW order and superconductivity, making in situ tuning of Fermi surfaces in nanodevices possible. Future studies using local-field-sensitive approaches at the nanoscale would also be beneficial for understanding the correlated charge orders and origin of TRSB. Techniques such as nitrogen-vacancy magnetometry, magnetic force microscopy and scanning superconducting quantum interference devices[232–234] could be helpful in this regard.

Kagome metal AM_6X_6

Although the AV_3Sb_5 family has provided a platform for learning about the complex orders and intertwining of orders in a kagome lattice, many questions remain unanswered. Another way to investigate the interplay of topology, correlation and magnetism in kagome materials is to expand investigations into kagome lattices housing other, more strongly magnetic elements. Another kagome metal family, AM_6X_6 (the '166' family) has attracted substantial attention due to its more prevalent magnetic properties and large chemical diversity; the A site can be an alkali, alkaline earth or rare earth metal, the M site can be a transition metal, such as Mn, Fe, Ni, V, Co or Cr, and the X site is typically a group IV element, such as Sn, Ge or Si. In this family (Fig. 4a), most of the AM_6X_6 compounds crystallize in centrosymmetric structures analogous to the CoSn structure type (or B35) that consists of graphite-like Sn nets and kagome nets of Co with Sn atoms centred in the hexagons. Depending on the relative positions of the A-site atoms and the capping of the transition metal atoms in the CoSn host structure, the whole structure of the intermetallic compound can be of hexagonal $HfFe_6Ge_6$-type (H-type) or hexagonal YCo_6Ge_6-type (Y-type, a disordered variant of the H-type).

Crystalline structures

The H-type $HfFe_6Ge_6$ (ref. 235) *P6/mmm* space group, with unit cell dimensions of $a = 5.065$ Å and $c = 8.058$ Å, is formed by 'stuffing' Hf atoms into the hexagonal voids of the FeGe (CoSn-type) framework, with alternating layers of filled and empty planes (Fig. 4a). This ordering of the Hf atoms in alternate layers doubles the unit cell along the *c* direction, where the kagome nets are separated by inequivalent Ge_3 layers and $HfGe_2$ layers. Many AM_6X_6 compounds such as RMn_6Sn_6 compounds (R = rare earth) possess the H-type $HfFe_6Ge_6$ structure (Fig. 4c).

The Y-type YCo_6Ge_6 structure[236] also crystallizes in the *P6/mmm* space group with unit cell dimensions of $a = 5.074$ Å, $c = 3.908$ Å, with Y atoms stuffed in the CoGe (CoSn-type) framework (Fig. 4a). In contrast to the order of the Hf atoms in the H-type, the Y atoms in the Y-type structure are occupationally disordered. Thus, although the H-type $HfFe_6Ge_6$ and Y-type YCo_6Ge_6 structures are similar, they are distinguishable by powder diffraction through the *d* spacing of the (001) reflection. Materials with Y-type YCo_6Ge_6 structures in AM_6X_6 compounds include $SmMn_6Ge_6$, $NdMn_6Ge_6$ and RFe_6Sn_6 (R = Y, Gd–Er)[237–240].

In addition to the H-type $HfFe_6Ge_6$ and Y-type YCo_6Ge_6 structures, some compounds crystallize in other structures with lower symmetry, such as the $HoFe_6Sn_6$-type[238,239] (*Immm* space group; materials include $YbFe_6Ge_6$, $LuFe_6Ge_6$), $TbFe_6Sn_6$-type[238,239] (*Cmcm* space group; materials include YFe_6Ge_6, $TbFe_6Ge_6$, $DyFe_6Ge_6$, $HoFe_6Ge_6$) and $GdFe_6Sn_6$-type[238] (*Pnma* space group). The large material family of AM_6X_6 compounds provides many opportunities to tune magnetic interactions and electronic correlations, depending on the interactions between the various elements and lattices. Various magnetic orders, metaphases and topological states have been observed and predicted.

Diverse magnetic states

Magnetism has been the most intensely investigated property in AM_6X_6 compounds over the past few decades, with diverse magnetic properties observed (unlike the AV_3Sb_5 family, which does not show obvious long-range magnetic order), including ferromagnetism, ferrimagnetism, antiferromagnetism, spin chirality and even non-magnetic behaviour. Different magnetic properties in different compounds are influenced by the interlayer and intralayer magnetic interaction of kagome lattices and sublattices of other elements.

Obvious magnetic textures generally appear in AM_6X_6 compounds with a kagome layer of Fe and Mn, such as RM_6X_6 compounds (R = rare earth; M = Mn, Fe; X = Ge,Sn)[38,74,238,239,241–246]. In these compounds, the magnetic atoms in the kagome lattice tend to have in-plane ferromagnetic ordering, and the total magnetism of the compounds changes depending on the interlayer magnetic exchange of the M–M lattice and M–R lattice. Typical examples are the RMn_6Sn_6 compounds with the $HfFe_6Ge_6$-type structure (Fig. 4c,d). When R is a magnetic rare earth element (R = Gd, Tb, Dy, Ho), there are strong interactions between the 4*f* electrons of the R atom and 3*d* electrons of the Mn atom[38,244–247]. These compounds have ferromagnetic layers of both R and M atoms, with ferromagnetic Mn–Mn inter-sublattice exchange, but strong antiferromagnetic Mn–R inter-sublattice coupling. As a result, the lanthanide and manganese sublattices order simultaneously, and the compounds present a collinear ferrimagnetic behaviour below their Curie transition temperatures (376–435 K)[245,246]. The magnetic order was reported to lie in-plane for R = Gd, whereas additional spin reorientation was also observed for R = Tb, Dy, Ho. In $TbMn_6Sn_6$ (refs. 244,248), the magnetic order is along the *c* axis at low temperature and deviates from it at room temperature. For R = Ho or Dy, a conical magnetic structure with magnetic order deviating by 45°–50° from the *c* axis was observed below 180–240 K (ref. 244).

In RMn_6Sn_6 compounds with R = Er, Tm and diamagnetic rare earth elements (R = Sc, Lu, Y), the magnetic coupling between R and Mn lattices is weak, and the compounds present a paramagnetic–antiferromagnetic transition with Néel temperature T_N of 340–384 K (refs. 245,246). For $ErMn_6Sn_6$ and $TmMn_6Sn_6$, the magnetic ordering of erbium and thulium sublattices introduces a second transition with ferrimagnetic (~75 K) and antiferromagnetic ordering (58 K)[246], respectively. However, in compounds with R = Sc, Y, Lu, the magnetism is dominated by the alignment of magnetic order in Mn sublattices[246]. These compounds were reported to have complex magnetic order due to interlayer magnetic interactions of nearest-neighbour and second-nearest-neighbour Mn kagome lattices, which introduces a transition with incommensurate antiferromagnetic ordering[249]. Below this transition (~333 K for YMn_6Sn_6), the Mn moments in YMn_6Sn_6 form the 'double flat spiral' structure in the absence of an applied magnetic field[250], where the in-plane moment of the Mn layer changes orientation with respect to each other, resulting in a spiral structure along the *c* axis. The spiral structure was also reported in $LuMn_6Sn_6$, $ScMn_6Sn_6$, $TmMn_6Sn_6$, and $ErMn_6Sn_6$ (refs. 249,251,252).

Compared with RMn_6Sn_6, the RMn_6Ge_6 family has fewer ferrimagnetic compounds. For example, ferrimagnetism was found for R = Nd, Sm (Curie temperature of 417–441 K)[240] whereas R = Dy–Yb, Sc, Y, Lu, Gd compounds show antiferromagnetic order (T_N increases for heavier rare earth elements)[238,253]. The relatively fewer ferrimagnetic compounds might be because of the shorter M–M interplanar distance in germanides, leading to enhanced M–M coupling that cannot be compensated by the M–R interaction when the ferrimagnetic order happens. Also, distinct from RMn_6X_6, in the iron compounds (RFe_6Sn_6 and RFe_6Ge_6), the strong easy *c*-axis anisotropy of the Fe lattices is reported to dominate the magnetic anisotropy, and most compounds have antiferromagnetic orders below $T_N > 400$ K (refs. 238,242).

In compounds with complex interlayer and intralayer interactions between R and Mn or Fe layers, magnetic reorientation and rich magnetic phases can also be generated by applying a magnetic field. For instance, the out-of-plane magnetic field (along the *c* axis) gradually tilts the magnetic moment in RMn_6Sn_6 (R = Dy, Tb, Ho, Gd) towards the *c* axis, whereas a metamagnetic transition happens in $ErMn_6Sn_6$ (ref. 38).

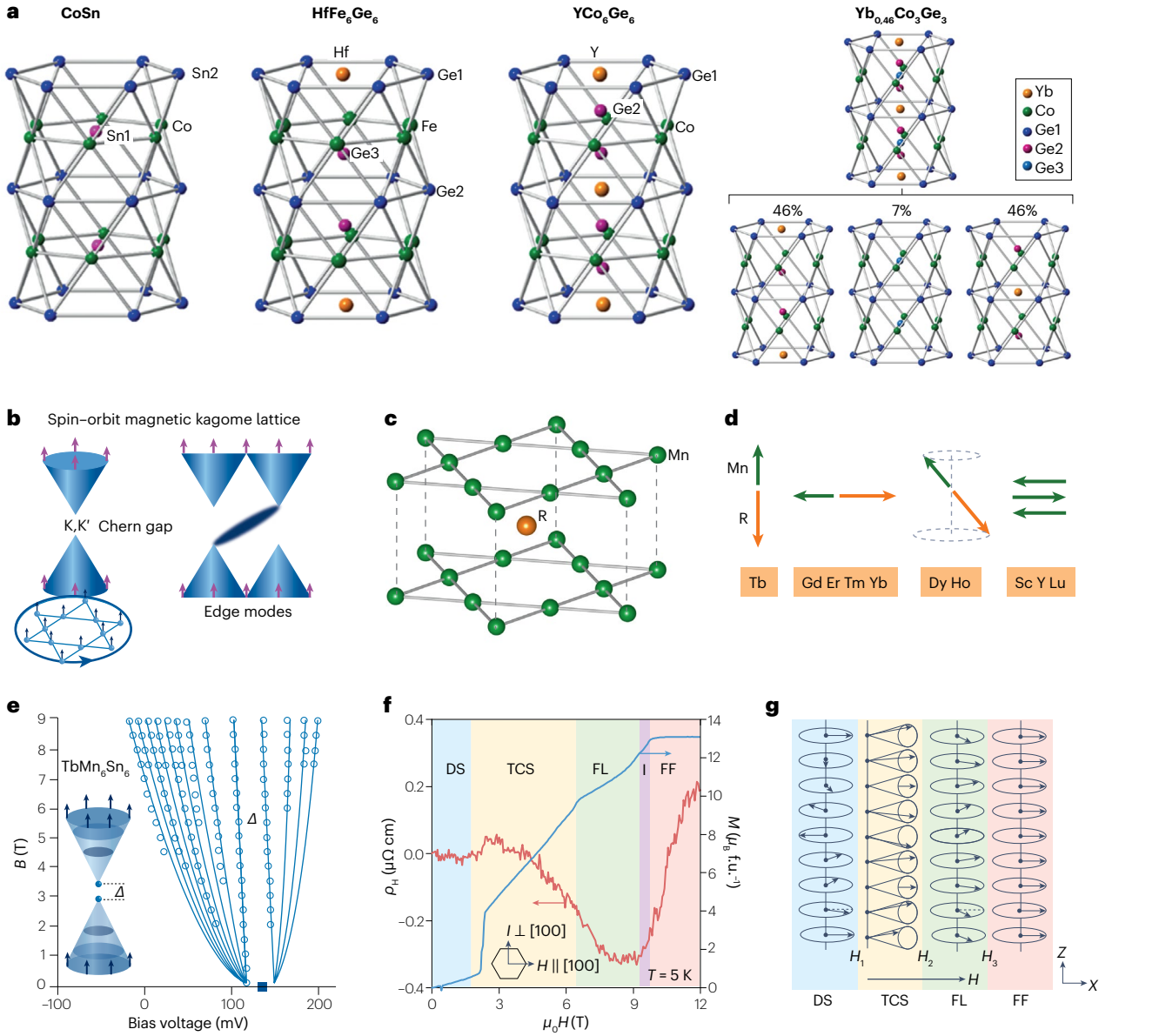

Fig. 4 | Crystal structures and physical properties in AM_6X_6 compounds. **a**, Crystal structures of CoSn, $HfFe_6Sn_6$ and YCo_6Ge_6 types. The $HfFe_6Sn_6$ structure type is an ordered variant of a 'stuffed' CoSn structure type. The YCo_6Ge_6 structure type is a disordered variant of a stuffed CoSn structure type. For clarity, the disorder of the YCo_6Ge_6 structure type is broken down into possible stuffing arrangements. **b**, Band structure of spin–orbit-coupled magnetic kagome lattice, where the spin-polarized Dirac bands opens a Chern gap with edge mode arising in the gap. **c**, Two kagome lattices in a unit cell of RMn_6Sn_6. **d**, The magnetic state of the R atom (orange arrow) and Mn (green arrow) in different RMn_6Sn_6 compounds. **e**, Landau fan data measured by scanning tunnelling microscopy (open circles) in $TbMn_6Sn_6$, fitted with the spin-polarized and Chern-gapped Dirac dispersion (solid line). The inset shows the schematic of Landau quantization of the Chern-gapped Dirac band. **f**, Hall resistivity ρ_H and magnetization M measured in YMn_6Sn_6 as a function of applied field H. The applied current (I) and magnetic field directions are shown in the inset. The magnetic structures change from a distorted spiral (DS) state to a transverse conical spiral (TCS), a fan-like (FL) state, a narrow intermediate (I) state and forced ferromagnetic (FF) state on increasing magnetic field. f.u., formula unit. **g**, Schematic of different field-induced magnetic structures. Part **a** adapted with permission from ref. 260, ACS. Parts **b** and **e** adapted with permission from ref. 37, Springer Nature Ltd. Parts **f, g** adapted with permission from ref. 250, AAAS.

In YMn_6Sn_6, it was reported that an increasing in-plane magnetic field (aligned with the kagome plane) can change the magnetic state from the distorted spiral state to a transverse conical spiral (TCS) phase, a fan-like state (a quadrupled structure along the c axis with spins deviating from in-plane magnetic field direction) and a forced ferromagnetic state[250,254] (Fig. 4f,g). In particular, a topological Hall effect was reported in YMn_6Sn_6 (ref. 84) and $TmMn_6Sn_6$ (ref. 85) without a field-driven skyrmion lattice, and the microscopic origin of this is proposed to originate from dynamic chiral fluctuation-driven non-zero spin chirality in TCS phase[84,85,250,255].

In addition to Mn/Fe-based compounds with rare earth R elements, distinct magnetic properties were reported in other compounds like the manganese stannides, in which ferromagnetic orders were attained by replacing the R element by alkali or alkaline earth elements with low concentrations of valance electron donors, such as Li, Mg or Ca. The Curie transition temperature is about 382 K for $LiMn_6Sn_6$ (easy plane parallel to kagome lattice) and 250–290 K for compounds with Mg and Ca (refs. 77,256). Moreover, unlike the Mn/Fe-based compounds, AM_6X_6 compounds with non-magnetic M-site variants (such as V-based compounds) allow the generation of non-magnetic kagome metals (such as YV_6Sn_6)[257] and compounds with weak magnetism (such as ScV_6Sn_6, GdV_6Sn_6)[257,258]. In the cobalt variants, $MgCo_6Ge_6$ (ref. 259) is paramagnetic, and weak magnetism was observed in $Yb_{0.5}Co_3Ge_3$ (refs. 260,261).

Topological states and flat bands

Based on the transition metal kagome lattice, AM_6X_6 compounds can host topological flat bands, vHSs and Dirac points in their band structure. In particular, the diverse magnetic coupling in these kagome magnets provides new opportunities to modulate the electronic bands and introduce new topological states and quantum phases.

The detection of all of these kagome band characters has been made through ARPES measurement in GdV_6Sn_6 (ref. 262), HoV_6Sn_6 (ref. 263), YCr_6Ge_6 (ref. 100) and YMn_6Sn_6 (ref. 99). Owing to the ideal kagome lattice and large bulk gap around Γ that allows topological surface states to be well separated (or unmixed) from bulk states, topological surface states were also detected in GdV_6Sn_6 and HoV_6Sn_6 (refs. 262,263). Note that the detection of topological surface states in these materials is distinct on different surface terminations and is sensitive to chemical doping on the surface. For YMn_6Sn_6, the vHSs, Dirac cone and flat band are observed to be quite close to the Fermi level[99]. YMn_6Sn_6 has in-plane ferromagnetic ordering of its Mn layer, but helical antiferromagnetic ordering along the *c* axis. Unlike the paramagnetic state, which normally has degenerate bulk bands, the spin degeneracy is theorized to be lifted in the magnetic state of YMn_6Sn_6 because of the ferromagnetic state with large SOC. Spin-polarized ARPES measurements are needed to confirm the band structure of magnetic YMn_6Sn_6. Besides these compounds, AV_6Sb_6 (A = K, Cs, Rb) with similar composition, but different stoichiometric ratios with AV_3Sb_5 family have been reported to be type-II Dirac nodal line semimetals, and superconductivity is realized under pressure[264,265].

Kagome materials that possess strong intrinsic SOC and out-of-plane ferromagnetism have the ability to realize non-trivial Chern phases, in which a gap is opened in the spin-polarized Dirac bands with spinless topological edge states lying in the gap[25,49,50,266] (Fig. 4b), as has been discussed in the section on the kagome lattice and basic physical properties. Taking advantage of the pure manganese kagome layers and a strong out-of-plane ferromagnetic order as well as a defect-free kagome lattice, a quantum-limited Chern phase was reported in $TbMn_6Sn_6$ using STM measurement[37] (Fig. 4e). Magnetic Landau quantization and localized edge states were detected in the Chern gap. In addition, $TbMn_6Sn_6$ presents an anomalous Hall effect with a prominent intrinsic contribution that is speculated to arise from the Berry curvature generated from Chern-gap Dirac fermions or other complex Dirac bands[37,267].

Similar to $TbMn_6Sn_6$, other RMn_6Sn_6 compounds with ferromagnetic kagome lattices, such as R = Gd–Er, are reported to host Chern-gapped Dirac fermions; these were also proposed in YMn_6Sn_6 (ref. 99). In RMn_6Sn_6 compounds (R = Gd–Er)[38], the existence of Chern-gapped Dirac fermions was studied through transport measurements of quantum oscillations with non-trivial Berry phases, as well as the large intrinsic anomalous Hall effect. The Dirac cone energy and gap size were reported to gradually decrease when R was changed from Gd to Er (ref. 38), highlighting the possibility of Chern-gap tuning based on tuning magnetic exchange coupling between the rare earth element with 4*f* electrons and the transition metal with 3*d* electrons. In addition to these compounds, introducing new 'high-entropy' phases by mixing multiple elements in the RMn_6Sn_6 system, such as $(Gd_{0.38}Tb_{0.27}Dy_{0.2}Ho_{0.15})Mn_6Sn_6$, can generate new magnetic transitions based on the competing magnetic interactions of the various elements at the mixed site[268]. It was reported that $(Gd_{0.38}Tb_{0.27}Dy_{0.2}Ho_{0.15})Mn_6Sn_6$ presents similar magnetic transitions to $TbMn_6Sn_6$ at high temperature, but new ferrimagnetic transitions with tilted magnetic moments (30°) around 90 K which were not seen in RMn_6Sn_6 (R = Gd, Tb, Dy, Ho). The high-entropy phase also shows an intrinsic anomalous Hall effect, suggesting possible Chern-gapped Dirac fermions[268].

CDW and structural transitions

Although some of the kagome magnets discussed above have strong correlations with saddle points and flat bands in electronic bands, no CDW has been observed in those systems so far. On the contrary, the CDW state and structural transitions were reported in several other AM_6X_6 compounds with specifically weak magnetism or a non-magnetic kagome lattice, including ScV_6Sn_6 ($HfFe_6Ge_6$-type)[258], $MgCo_6Ge_6$ ($HfFe_6Ge_6$-type)[259], and in $Yb_{0.5}Co_3Ge_3$ (a hybrid structure of YCo_6Ge_6-type and CoSn-type)[260,261]. This is similar to the case of the AV_3Sb_5 family discussed above, which also has weak or non-magnetic kagome lattices, although the details of the transitions and ground states are different, suggesting that a competition between the correlated and magnetic ground states generally exists in kagome lattices.

Like the AV_3Sb_5 family, ScV_6Sn_6 hosts a vanadium kagome lattice with a partly filled *d* orbital. A transition signal around 92 K was observed in resistivity, magnetization and heat capacity, which is confirmed to be a CDW transition by single-crystal X-ray diffraction[258]. Unlike AV_3Sb_5, which hosts $2\times2\times2$ or $2\times2\times4$ CDW orders, the distorted lattices in ScV_6Sn_6 were reported to possess $\sqrt{3}\times\sqrt{3}\times3$ CDW orders. In addition, ScV_6Sn_6 shows strong modulated displacement of the Sc and Sn atoms in CDW state, but weak displacements of the V atoms, distinct from the lattice rearrangement dominated by V net displacement that is found in AV_3Sb_5. The partly filled *d*-orbital kagome bands were proposed to be related to the CDW order. ARPES measurement of the band structure shows the existence of vHS around the Fermi level and Dirac bands associated with a topologically non-trivial surface state. However, in contrast to the AV_3Sb_5 family, it is widely observed that the vHS remains intact during the CDW transition in ScV_6Sn_6, indicating a marginal role in the electronic instability of the V kagome lattice. Instead, a large charge-order gap is detected on the bands dominated by planar Sn associated with reconstruction of the Fermi surface, and a partial gap opening in the DOS around the Fermi level is detected by STM. Distinct from the electronically driven mechanism from Fermi surface nesting, the origin of CDW order is widely proposed to be dominated by electron–phonon interaction[102,269–276]. For example, Raman studies detected multiple phonon modes associated with the CDW transition[102,272,273], and softening of a flat phonon mode related to an out-of-plane Sn vibration is observed by hard X-ray diffraction[270]. In addition, a theoretical study proposed a large lattice instability with abundant CDW orders in ScV_6Sn_6 due to a small Sc atomic radius[277], and before the appearance of $\sqrt{3}\times\sqrt{3}\times3$ order, an energetically favoured $\sqrt{3}\times\sqrt{3}\times2$ CDW order has been observed by X-ray experiments[271].

It was also found that the CDW order is sensitive to the physical and chemical pressure[273] and is reported to disappear around 2.4 GPa without the appearance of superconductivity[278]. Unlike AV_3Sb_5, there is no rotation symmetry breaking in the CDW state. However, like in AV_3Sb_5, μSR detected TRSB below the CDW transition, implying that hidden magnetism and unconventional charge order may be present in ScV_6Sn_6 (ref. 279), but more investigation is needed.

Compared with AV_3Sb_5 and ScV_6Sn_6, the structural transition observed in the Co-based kagome compounds is quite different. $Yb_{0.5}Co_3Ge_3$ crystallizes in the *P6/mmm* space group with one kagome layer in the unit cell at room temperature[260]. A phase transition associated with a resistivity anomaly was observed in $Yb_{0.5}Co_3Ge_3$ around 95 K. Below this transition, the Yb and Ge atoms retain their geometries, whereas the Co atoms distort the kagome plane by 'twisting' the triangles in opposite directions between two neighbouring kagome lattices, resulting in a doubling of the unit cell along the *c* axis, crystallizing in the $P6_3/m$ space group that breaks C_6 rotation symmetry[261]. $MgCo_6Ge_6$ has similar transitions with twisting of the kagome lattice at low temperature[280], and the structure changes from the *P6/mmm* ($HfFe_6Ge_6$-type) space group at room temperature to $P6_3/mcm$ at 100 K (ref. 259). This twisted structure was proposed to be related to interaction of Co–Ge atoms and splitting of the 3*d* orbital in Co. Unlike AV_3Sb_5 and ScV_6Sn_6, which have clear magnetization variation commensurate with the structural transition, there is no change of magnetization during the structural transition in $Yb_{0.5}Co_3Ge_3$ and $MgCo_6Ge_6$. This unusual feature is not yet fully understood, but it may be related to the particular twisting of Co lattices. And whereas a CDW transition without related magnetic transition has been reported in other kinds of correlated materials (such as $NdNiC_2$)[281,282], $Yb_{0.5}Co_3Ge_3$ shows a weak magnetic transition signal around 18–25 K, along with the appearance of negative magnetoresistance below the transition temperature[261], meaning that there is further unresolved complexity in the low-temperature state. It is also worth noting that some materials in the RT_3X_2 (R = rare earth, T = transition metal, X = Si, Ga, B) kagome family (132 family) with similar twisted structures are observed to be superconductors, but without a temperature-dependent structural phase transition. These include $LaRu_3Si_2$, $LaIr_3Ga_2$ and YRu_3Si_2 (refs. 283–286). It may be interesting to explore whether the superconductivity can appear in Co-based AM_6X_6 compounds with their structural transition at ultralow temperatures, or whether it can arise on suppression of the structural transition. Chemical doping and high-pressure approaches might be used to explore the structural and magnetic phase transitions and possible superconductivity in $Yb_{0.5}Co_3Ge_3$ and $MgCo_6Ge_6$.

The trigonally distorted kagome system (Nb_3X_8, X = Cl, Br, I)

One highly interesting structural modulation of the ideal kagome lattice is the trigonal distortion, also called the 'breathing' kagome lattice, described above (Fig. 1c). An important example material family with the breathing kagome lattice is the kagome insulator Nb_3X_8 (X = Cl, Br, I)[40,287], which has very different physical properties from the AV_3Sb_5 (A = K, Rb, Cs) and '166' materials.

Crystal structures

The Nb_3X_8 family is also a vdW type material and has layered structures that are readily exfoliated, more easily achieving ultrathin flakes than the AV_3Sb_5 family, as individual layers are very weakly coupled through vdW interactions[39,288]. Nb_3Cl_8 and Nb_3Br_8 have been experimentally demonstrated to undergo a temperature-dependent structural phase transition: at high temperature, the α-phase has space group $P\bar{3}m1$, but at low temperature the exact phase is not fully understood[39,289,290]. Nb_3Br_8 has a transition temperature above room temperature, and its low-temperature phase has space group of $R\bar{3}m$ (β-phase)[39] (Fig. 5b). However, Nb_3Cl_8 has transition temperature around 90 K, and its corresponding low-temperature phase is still under debate. A space group of *R*3 in Nb_3Cl_8 was reported by NMR measurement at 78 K (ref. 289), whereas another work reported the space group of *C*2/*m* by neutron diffraction at 10 K (ref. 290). Later, investigation of the intermediate compound $Nb_3Cl_4Br_4$ via single-crystal X-ray diffraction[39] indicated that Nb_3Cl_8 has the space group of $R\bar{3}m$, the same as the β-phase of Nb_3Br_8. Both α- and β-phases have the same single-layer structure, but they have different stacking orders, hence the different unit cells (Fig. 5b). A single layer of Nb_3X_8 shows the breathing kagome structure formed by the Nb atoms, where three Nb atoms are trimerized through strong metal–metal bonds (Fig. 5a). Each Nb atom is under a distorted octahedral environment of X atoms, and each layer has a sheet of Nb atoms that is sandwiched between two sheets of X atoms. In addition, the two sheets of X atoms are not equivalent, resulting in the breaking of inversion symmetry in a single layer (non-centrosymmetric). The α-phase contains a unit cell of two layers with the second layer being an inversion of the first layer. The β-phase contains six layers with each layer resulting from the inversion operation of the previous layer with a translation, hence glide planes are present. In addition, both the α- and β-phases have inversion centres located at every vdW gap, and as a result even-layered Nb_3X_8 preserves inversion symmetry whereas odd-layered Nb_3X_8 breaks it. Finally, Nb_3I_8 shows the same crystal structure as Nb_3Br_8 (β-phase) at room temperature, but there are as yet no reports of a transition; it is likely that it undergoes the same transition with Nb_3Cl_8 and Nb_3Br_8 at higher temperature, but more study is necessary.

Magnetic properties

Nb_3Cl_8 and Nb_3Br_8 in both bulk and powder forms undergo a phase transition from a paramagnetic state to a non-magnetic singlet state[39], accompanying the structural transition[39]. Measurements of magnetic susceptibility as a function of temperature reveal that the transition temperature of Nb_3Cl_8 is ~90 K and increases when Cl is substituted by Br, and reaches ~380 K for Nb_3Br_8 (ref. 39) (Fig. 5c). It is worth noting that at room temperature, bulk Nb_3Cl_8 is paramagnetic with a unit cell containing two Cl–Nb–Cl sheets, whereas bulk Nb_3Br_8 is non-magnetic with six Br–Nb–Br sheets in a unit cell. There are also upturned tails on cooling the samples to 10–20 K (Fig. 5c); it was proposed that these features originate from defect spins induced by broken singlets or trapped high-temperature phases during synthesis, as the tails are sample-dependent rather than material-intrinsic[39]. Although there are no magnetic experimental studies yet on Nb_3I_8, either in bulk or powder, from theoretical calculations it is expected that it has the similar magnetic transition[288,291] to Nb_3Cl_8 and Nb_3Br_8, but at a higher temperature.

One question arising from the magnetic properties that have not been characterized down to the 2D limit is whether the transition temperature changes with thickness as the flakes become thinner, and whether few-layer flakes possess different magnetic properties from the bulk. Theoretical calculations predict that the ground state of Nb_3X_8 in monolayer form is ferromagnetic[291,292]. In Nb_3I_8, some studies also predict that it has layer-dependent magnetism; for monolayer and bulk, it is ferromagnetic, but for bilayer and trilayer, it is antiferromagnetic owing to interlayer coupling. In addition, different theoretical

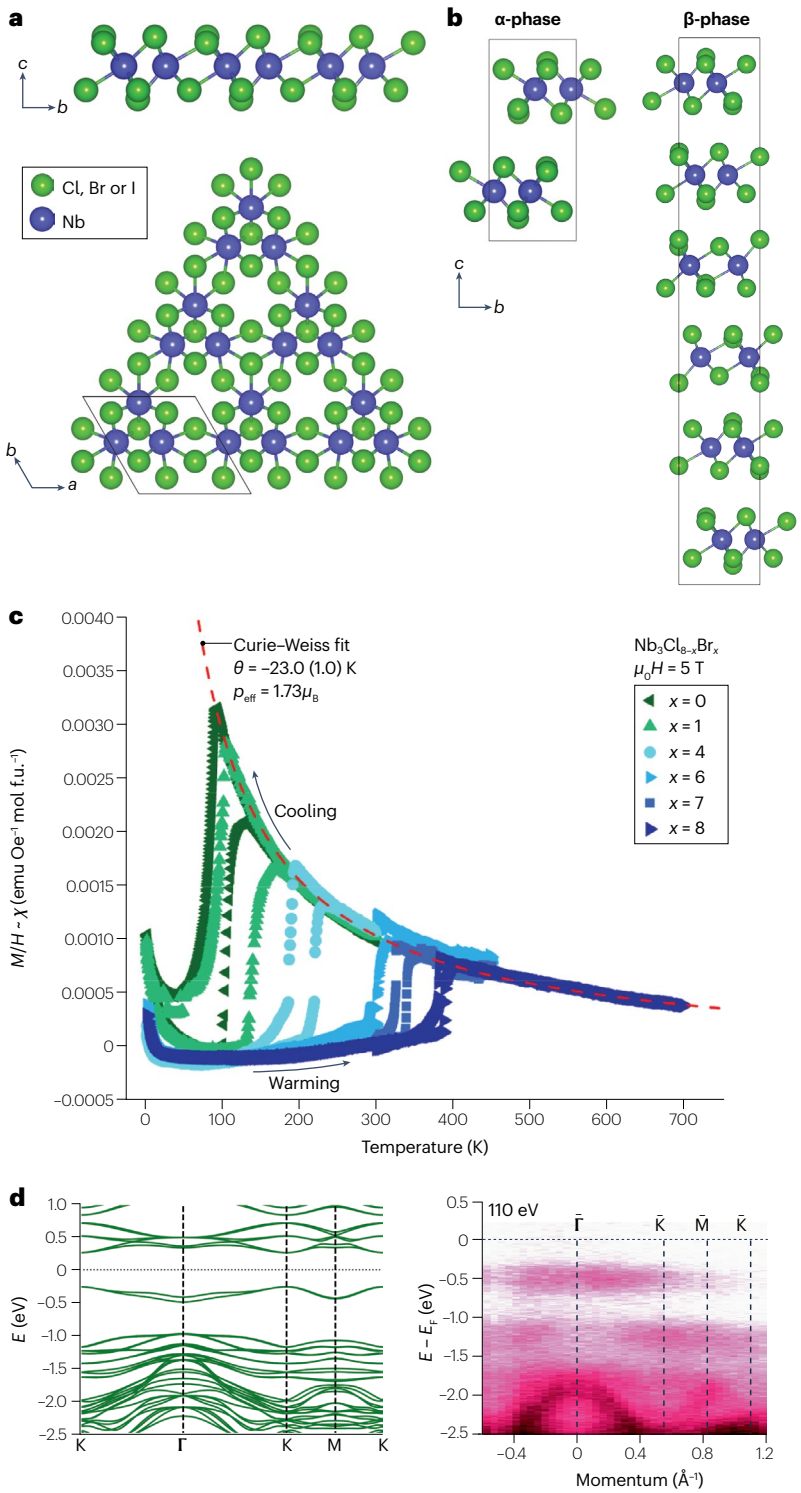

Fig. 5 | Crystal structure and physical properties of Nb_3X_8. **a**, Single-layer structure of Nb_3X_8 and corresponding *ab* plane structure. **b**, Crystal structures for α-phase ($P\bar{3}m1$) and β-phase ($R\bar{3}m$) of Nb_3X_8. **c**, Temperature-dependent magnetic susceptibility χ ($\chi = M/H$, M is magnetization; H is magnetic field intensity) of $Nb_3Cl_{8-x}Br_x$. θ, Weiss temperature; p_{eff}, effective moment. **d**, Flat band of Nb_3I_8 bulk measured by angle-resolved photoemission spectroscopy; the left panel is the calculated band structure. Part **c** adapted with permission from ref. 39, ACS. Part **d** adapted with permission from ref. 300 under a Creative Commons licence CC BY 4.0.

calculations yield very different Curie temperatures for monolayer Nb_3I_8: 307.5 K in ref. 291 compared with 87 K in ref. 292. It is worth noting that these theoretical calculations for the Nb_3X_8 family only used the Ising spin model (easy axis of spin orientation is along the *z* axis)[291,292] and treated the magnetic moment as carried by individual Nb atoms. In contrast, it is also proposed that owing to the existence of Nb trimerization in the Nb_3X_8 breathing kagome lattice, each Nb trimer has seven *d* orbitals and yields a single $S = 1/2$ magnetic moment, and thus the breathing kagome lattice becomes the triangular lattice[93,289,293]. Based on this idea, theoretical calculations predict the possibility of

an all-in antiferromagnetic spin structure[293] or a quantum spin liquid state in monolayer Nb_3Cl_8 (ref. 93). Given the discrepancies of the properties predicted, more detailed studies on the magnetization of bulk and few-layer Nb_3X_8, including μSR as was done for the AV_3Sb_5 family, are required to elucidate the question of their ground magnetic state.

Correlations and obstructed atomic insulating states

Most ab initio theoretical calculations show a metallic band structure of Nb_3Cl_8 and Nb_3Br_8 in their bulk form[41,42,290,294]. However, in both transport and ARPES measurements, they are proven to be insulating[42,294,295] with bandgaps ~1 eV. Such a large discrepancy between theoretical and experimental results indicates the presence of non-trivial effects from the kagome lattice. One possible origin of this abnormal insulating state is that Nb_3Cl_8 and Nb_3Br_8 may have very strong electron correlations. They are predicted to be Mott insulators, with the kagome flat band lying near the Fermi level splitting into two bands, the so-called upper and lower Hubbard bands, yielding the observed insulating state[41,42,293]. Such an explanation agrees well with recent ARPES measurement in Nb_3Cl_8 bulk[42].

Obstructed atomic insulator theory[296,297] can also explain this abnormal insulating state. It predicts that in β-phase Nb_3Br_8 and Nb_3I_8, there are centres of charges not localized on the atoms but sitting in the vdW gaps in every other layer. Therefore, whereas Nb_3Br_8 and Nb_3I_8 flakes with an odd number of layers can be metallic, flakes with an even number of layers can be either metallic or insulating based on the termination conditions. If the charge centres are exposed on the surface as a trivial surface state, the flakes can be metallic, but if the charge centres are buried inside the vdW gap, they are insulating. Note that the obstructed atomic insulator theory is based on density functional theory without taking electron correlation into account. Similar metallic (monolayer layer) and insulating states (bilayer) are also reported in other works that do not consider electronic correlation, and a Mott-insulating state is found when strong electron correlations are included[41,298]. In Nb_3Br_8, it was also calculated that the interlayer coupling between neighbouring layers forms strong and weak coupling bonds alternatively, which could give rise to the layer-dependent electronic properties[41,298]. Therefore, β-phase Nb_3Br_8 and Nb_3I_8 may be strongly correlated systems in addition to their atomic obstructed insulator nature[298].

In the absence of strong correlations and obstructed atomic insulator theory, both theoretical calculations and ARPES experiments show an insulating state at room temperature in Nb_3I_8 (β-phase)[291]. The band structure is also predicted to be thickness-dependent, being metallic in the monolayer, insulating for a bilayer and metallic for a trilayer, with corresponding thickness-dependent magnetic properties[291].

Many of these electronic-band-structure results are calculated without including SOC. The theoretical calculations that do so also predict that on introducing SOC, the monolayer of the Nb_3X_8 family shows a spontaneous valley polarization as large as ~100 meV (ref. 299). Among this family, Nb_3I_8 is proposed to be a good platform for investigating a valley Hall effect. Nb_3Cl_8 and Nb_3Br_8 are less suitable because their spin-down bands are predicted to be in the gap of the spin-up bands.

Flat bands

Although there are different predications of the electronic band structures, a common feature in many studies is the prominent flat band in the Nb_3X_8 family. As introduced above, flat bands exist in the ideal kagome lattice, but the flat band is extremely isolated in the trigonally distorted lattice. Recent ARPES measurements showed flat bands below the Fermi level in Nb_3Cl_8 bulk, and Nb_3I_8 bulk (Fig. 5d) at room temperature[300]. The flat band in Nb_3Cl_8 bulk lies at around 0.72 eV below the Fermi level with a bandwidth of 0.28 eV (ref. 42). Note that the crystal structure of Nb_3Cl_8 is α-phase whereas Nb_3I_8 is β-phase at room temperature, having a different glide-plane symmetry between layers. This indicates that the flat band is robust against the layer stacking situation, probably because of the weak vdW interaction between layers.

Although the ARPES results confirm the presence of the flat band in these materials, it has not yet been studied via transport because of their highly insulating state, making access to it much more difficult. There are at least two alternative ways to overcome this obstacle: first, by making thinner Nb_3X_8 flakes, as it has been theorized that at least monolayer Nb_3X_8 will be metallic while preserving its flat band near the Fermi level; second, by gate tuning — although bilayer and thicker Nb_3X_8 might still be insulating, these systems should also be gate-tunable, allowing the different filling states of the flat band to be investigated. And whereas the Nb_3X_8 family shows intriguing band structures and abnormal magnetic properties in bulk, studies of their layer-dependent properties are few. They showed a unique property when integrated into heterostructures: for instance, Nb_3Br_8 was adopted as a barrier layer in a Josephson junction[301], forming a $NbSe_2/Nb_3Br_8/NbSe_2$ heterostructure, and displayed the field-free Josephson diode effect (non-reciprocal superconductivity without magnetic field). These observations indicate that Nb_3X_8 family hosts more exotic physical properties, especially in their few-layer forms, and their easy exfoliation and ability to be integrated into heterostructures make them an ideal platform to study the isolated kagome flat band, Mott-insulating state and trigonal distortion. Manufactured correlation through the formation of moiré superlattices via twisted stacking is another important structural parameter that can be tuned in this family. Their study is an extremely fertile area for deep investigation of correlated physics.

Outlook

Studies from recent years have shown many kagome materials with different kinds of features, ranging from metallic to insulating, non-magnetic to hosting complex magnetic textures, and relatively weak electron correlation to very strong correlation (Table 1). One common feature observed in kagome materials is the sensitivity and tunability of many properties, such as topological surface states, charge orders, superconductivity and magnetism, which can be tuned by diverse approaches including chemical or electrical doping, strain and pressure. Another feature is the surface termination dependence of the physical properties, where the surface state of kagome bands might be influenced by interlayer interactions that vary on different terminations. The kagome lattice is a platform providing substantial material diversity that can realize broad physical research directions.

The intertwining and tuning of different ordered states are still important directions that need further investigation. The appearance of ordered states in materials is complex, and clear conclusions are difficult to obtain because they are very sensitive to the electronic state around the Fermi level. Nonetheless, experimental and theoretical studies suggest some clues for understanding the various ordered states. As discussed above, around the van Hove filling, different electronic orders can appear depending on the strength of different electron interactions. The intertwining and competition of many ordered states (such as superconducting state, CDW order, nematic or smectic phases) appear in materials with relatively weak or intermediate electron-correlation strength, such as in AV_3Sb_5 and ScV_6Sn_6. For AV_3Sb_5,

although the relation of electronic orders and superconductivity has been studied extensively, the explicit charge-ordered states breaking TRS and the nature of its superconductivity remain elusive, which is a challenging but essential topic for further research.

The formation of charge-instability-induced states (such as CDWs) in kagome materials is mostly observed in materials with weak magnetism, such as ScV_6Sn_6 and AV_3Sb_5. A short-range CDW order was also reported in the antiferromagnetic state of correlated kagome metal FeGe (ref. 302), which is proposed to arise from vHSs-driven Fermi surface instability near the Fermi level. The coupling of magnetic orders and electron correlations is another important direction to explore in future. For example, it would be good to understand the relationship between CDW and magnetic order (not only their competition, but also how they combine to influence, for example, superconductivity), as well as investigating intriguing quantum states, such as spin density waves and chiral spin orders in the magnetic states of materials with strong Fermi surface nesting around the Fermi level.

Another important direction is the coupling of topology with other orders, which can lead to unconventional phases. The combination of topology and magnetism can induce new topological states in magnetic kagome materials, such as Chern phases in the RMn_6Sn_6 family with strong SOC, associated with an anomalous Hall effect and anomalous thermal Hall[241,303] effect induced by large Berry curvature. These are just the beginning: topological kagome magnets provide opportunities for investigations of phenomena, such as the quantum anomalous Hall effect, fractional quantum Hall effect and Weyl states. In addition, kagome magnets are also promising for exploring spin transport and spintronics, including charge–spin conversion and spin–orbit-torque-based spintronic devices that use spin-polarized topological bands and strong SOC, as well as magnon dynamics and skyrmion formation from exchange coupling tuning in kagome magnets. The diverse magnetism of the AM_6X_6 family can provide a good platform for investigating the relation of topological states and magnetic coupling.

Moreover, based on the topological states and electron correlations, there is a great opportunity to explore unconventional and topological superconductivity in kagome materials, either using their intrinsic superconductivity or through the proximity effect. In fact, there are many kagome compounds with intrinsic superconductivity that await more exploration, such as MgB_3 (ref. 304), $CeRu_2$ (refs. 305,306) and the RT_3X_2 (R = rare earth, T = transition metal, X = Si, Ga, B)[307,308] family, which have recently been proposed to possess the expected flat bands, Dirac cones and vHSs[284,309]. These kagome superconductors can provide a new platform for investigating the interplay of topology, correlation and magnetism. In addition, unconventional superconductivity can be studied by inducing superconductivity in intrinsically non-superconducting kagome materials based on Josephson junctions or superconducting heterostructures. For example, unconventional pairing and Majorana states, superconducting topological boundary states, long-lived transport of spin-triplet pairing based on non-collinear spins or inhomogeneous magnetization in kagome magnets, and more, can be studied.

With clear flat bands observed in many kagome materials, the associated quantum phases will be another critical focus. Partial filling of flat bands can induce quantum phases such as Mott-insulating states, non-trivial Chern topology, unconventional superconductivity and a fractional quantum Hall effect. Materials with isolated flat bands (such as Nb_3X_8 compounds) have potential to realize these states by modulation of the filling of bands and engineering of the band structure through chemical doping, electrostatic tuning or mechanical modification. In addition, kagome antiferromagnets with spin–orbit-coupled Mott-insulating states might be candidates for investigating a quantum spin liquid ground state based on the frustration of strongly localized magnetic moments. Finally, the multitude of exotic phenomena that these materials possess makes them very interesting for integration into nanoscale electronic devices, such as heterostructures of layered kagome materials.

Published online: 27 September 2023

References

1. Fradkin, E., Kivelson, S. A. & Tranquada, J. M. Colloquium: Theory of intertwined orders in high temperature superconductors. *Rev. Mod. Phys.* **87**, 457–482 (2015).
2. Chen, C. W., Choe, J. & Morosan, E. Charge density waves in strongly correlated electron systems. *Rep. Prog. Phys.* **79**, 084505 (2016).
3. Paschen, S. & Si, Q. Quantum phases driven by strong correlations. *Nat. Rev. Phys.* **3**, 9–26 (2021).
4. Fradkin, E. Electronic liquid crystal phases in strongly correlated systems. In *Modern Theories of Many-Particle Systems in Condensed Matter Physics, Lecture Notes in Physics* Vol. 843 (eds Cabra, D. C. et al.) (Springer, 2012).
5. Andrei, E. Y. & MacDonald, A. H. Graphene bilayers with a twist. *Nat. Mater.* **19**, 1265–1275 (2020).
6. Balents, L., Dean, C. R., Efetov, D. K. & Young, A. F. Superconductivity and strong correlations in moiré flat bands. *Nat. Phys.* **16**, 725–733 (2020).
7. Si, Q. & Steglich, F. Heavy fermions and quantum phase transitions. *Science* **329**, 1161–1166 (2010).
8. Cao, Y. et al. Correlated insulator behaviour at half-filling in magic-angle graphene superlattices. *Nature* **556**, 80–84 (2018).
9. Shores, M. P., Nytko, E. A., Bartlett, B. M. & Nocera, D. G. A structurally perfect $S=1/2$ kagomé antiferromagnet. *J. Am. Chem. Soc.* **127**, 13462–13463 (2005).
10. Norman, M. R. Colloquium: herbertsmithite and the search for the quantum spin liquid. *Rev. Mod. Phys.* **88**, 041002 (2016).
11. Anderson, P. W. The resonating valence bond state in La_2CuO_4 and superconductivity. *Science* **235**, 4793 (1987).
12. Balents, L. Spin liquids in frustrated magnets. *Nature* **464**, 199–208 (2010).
13. Morali, N. et al. Fermi-arc diversity on surface terminations of the magnetic Weyl semimetal $Co_3Sn_2S_2$. *Science* **365**, 1286–1291 (2019).
14. Liu, D. F. et al. Magnetic Weyl semimetal phase in a kagomé crystal. *Science* **365**, 1282–1285 (2019).
15. Kang, M. et al. Dirac fermions and flat bands in the ideal kagome metal FeSn. *Nat. Mater.* **19**, 163–169 (2020).
16. Liu, Z. et al. Orbital-selective Dirac fermions and extremely flat bands in frustrated kagome-lattice metal CoSn. *Nat. Commun.* **11**, 4002 (2020).
17. Kang, M. et al. Topological flat bands in frustrated kagome lattice CoSn. *Nat. Commun.* **11**, 4004 (2020).
18. Hou, Z. et al. Observation of various and spontaneous magnetic skyrmionic bubbles at room temperature in a frustrated kagome magnet with uniaxial magnetic anisotropy. *Adv. Mater.* **29**, 1701144 (2017).
19. Hou, Z. et al. Creation of single chain of nanoscale skyrmion bubbles with record-high temperature stability in a geometrically confined nanostripe. *Nano Lett.* **18**, 1274–1279 (2018).
20. Cable, J. W., Wakabayashi, N. & Radhakrishna, P. Magnetic excitations in the triangular antiferromagnets Mn_3Sn and Mn_3Ge. *Phys. Rev. B* **48**, 6159 (1993).
21. Yang, H. et al. Topological Weyl semimetals in the chiral antiferromagnetic materials Mn_3Ge and Mn_3Sn. *New. J. Phys.* **19**, 015008 (2017).
22. Nakatsuji, S., Kiyohara, N. & Higo, T. Large anomalous Hall effect in a non-collinear antiferromagnet at room temperature. *Nature* **527**, 212–215 (2015).
23. Zhang, H., Feng, H., Xu, X., Hao, W. & Du, Y. Recent progress on 2D kagome magnets: binary T_mSn_n (T=Fe, Co, Mn). *Adv. Quantum Technol.* **4**, 2100073 (2021).
24. Kanagaraj, M., Ning, J. & He, L. Topological $Co_3Sn_2S_2$ magnetic Weyl semimetal: from fundamental understanding to diverse fields of study. *Rev. Phys.* **8**, 100072 (2022).
25. Yin, J.-X., Lian, B. & Hasan, M. Z. Topological kagome magnets and superconductors. *Nature* **612**, 647–657 (2022).
26. Ortiz, B. R. et al. New kagome prototype materials: discovery of KV_3Sb_5,RbV_3Sb_5, and CsV_3Sb_5. *Phys. Rev. Mater.* **3**, 094407 (2019).
27. Neupert, T., Denner, M. M., Yin, J. X., Thomale, R. & Hasan, M. Z. Charge order and superconductivity in kagome materials. *Nat. Phys.* **18**, 137–143 (2022).
28. Chen, H., Hu, B., Ye, Y., Yang, H. & Gao, H.-J. Superconductivity and unconventional density waves in vanadium-based kagome materials AV_3Sb_5. *Chin. Phys. B* **31**, 097405 (2022).
29. Jiang, K. et al. Kagome superconductors AV_3Sb_5 (A=K, Rb, Cs). *Natl Sci. Rev.* **10**, nwac199 (2022).
30. Zhao, H. et al. Cascade of correlated electron states in the kagome superconductor CsV_3Sb_5. *Nature* **599**, 216–221 (2021).
31. Chen, H. et al. Roton pair density wave in a strong-coupling kagome superconductor. *Nature* **599**, 222–228 (2021).

32. Ortiz, B. R. et al. CsV_3Sb_5: a Z_2 topological kagome metal with a superconducting ground state. *Phys. Rev. Lett.* **125**, 247002 (2020).
33. Ortiz, B. R. et al. Superconductivity in the Z_2 kagome metal KV_3Sb_5. *Phys. Rev. Mater.* **5**, 034801 (2021).
34. Yang, S. Y. et al. Giant, unconventional anomalous Hall effect in the metallic frustrated magnet candidate, KV_3Sb_5. *Sci. Adv.* **5**, eabb6003 (2020).
35. Yu, F. H. et al. Concurrence of anomalous Hall effect and charge density wave in a superconducting topological kagome metal. *Phys. Rev. B* **104**, L041103 (2021).
36. Wang, L. et al. Anomalous Hall effect and two-dimensional Fermi surfaces in the charge-density-wave state of kagome metal RbV_3Sb_5. *J. Phys. Mater.* **6**, 02LT01 (2023).
37. Yin, J. X. et al. Quantum-limit Chern topological magnetism in $TbMn_6Sn_6$. *Nature* **583**, 533–536 (2020).
38. Ma, W. et al. Rare earth engineering in RMn_6Sn_6 (R=Gd-Tm, Lu) topological kagome magnets. *Phys. Rev. Lett.* **126**, 246602 (2021).
39. Pasco, C. M., El Baggari, I., Bianco, E., Kourkoutis, L. F. & McQueen, T. M. Tunable magnetic transition to a singlet ground state in a 2D van der Waals layered trimerized kagomé magnet. *ACS Nano* **13**, 9457–9463 (2019).
40. Magonov, S. N. et al. Scanning tunneling and atomic force microscopy study of layered transition metal halides Nb_3X_8 (X=Cl, Br, I). *J. Am. Chem. Soc.* **115**, 2495–2503 (1993).
41. Zhang, Y., Gu, Y., Weng, H., Jiang, K. & Hu, J. Mottness in two-dimensional van der waals Nb_3X_8 monolayer (X=Cl, Br, and I). *Phys. Rev. B* **107**, 035126 (2023).
42. Gao, S. et al. Mott insulator state in a van der Waals flat-band compound. Preprint at https://doi.org/10.48550/arXiv.2205.11462 (2022).
43. Wang, W. S., Li, Z. Z., Xiang, Y. Y. & Wang, Q. H. Competing electronic orders on kagome lattices at van Hove filling. *Phys. Rev. B* **87**, 115135 (2013).
44. Kiesel, M. L. & Thomale, R. Sublattice interference in the kagome Hubbard model. *Phys. Rev. B* **86**, 121105 (2012).
45. Kiesel, M. L., Platt, C. & Thomale, R. Unconventional Fermi surface instabilities in the kagome Hubbard model. *Phys. Rev. Lett.* **110**, 126405 (2013).
46. Guo, H. M. & Franz, M. Topological insulator on the kagome lattice. *Phys. Rev. B* **80**, 113102 (2009).
47. Bolens, A. & Nagaosa, N. Topological states on the breathing kagome lattice. *Phys. Rev. B* **99**, 165141 (2019).
48. Green, D., Santos, L. & Chamon, C. Isolated flat bands and spin-1 conical bands in two-dimensional lattices. *Phys. Rev. B* **82**, 075104 (2010).
49. Xu, G., Lian, B. & Zhang, S. C. Intrinsic quantum anomalous Hall effect in the kagome lattice $Cs_2LiMn_3F_{12}$. *Phys. Rev. Lett.* **115**, 186802 (2015).
50. Tang, E., Mei, J. W. & Wen, X. G. High-temperature fractional quantum Hall states. *Phys. Rev. Lett.* **106**, 236802 (2011).
51. Sun, K., Yao, H., Fradkin, E. & Kivelson, S. A. Topological insulators and nematic phases from spontaneous symmetry breaking in 2D Fermi systems with a quadratic band crossing. *Phys. Rev. Lett.* **103**, 046811 (2009).
52. Liu, Q., Yao, H. & Ma, T. Spontaneous symmetry breaking in a two-dimensional kagome lattice. *Phys. Rev. B* **82**, 045102 (2010).
53. Wen, J., Rüegg, A., Wang, C. C. J. & Fiete, G. A. Interaction-driven topological insulators on the kagome and the decorated honeycomb lattices. *Phys. Rev. B* **82**, 075125 (2010).
54. Zhu, W., Gong, S. S., Zeng, T. S., Fu, L. & Sheng, D. N. Interaction-driven spontaneous quantum Hall effect on a kagome lattice. *Phys. Rev. Lett.* **117**, 096402 (2016).
55. Ren, Y., Zeng, T. S., Zhu, W. & Sheng, D. N. Quantum anomalous Hall phase stabilized via realistic interactions on a kagome lattice. *Phys. Rev. B* **98**, 205146 (2018).
56. Tanaka, A. & Ueda, H. Stability of ferromagnetism in the Hubbard model on the kagome lattice. *Phys. Rev. Lett.* **90**, 067204 (2003).
57. Katsura, H., Maruyama, I., Tanaka, A. & Tasaki, H. Ferromagnetism in the Hubbard model with topological/non-topological flat bands. *Europhys. Lett.* **91**, 57007 (2010).
58. Pollmann, F., Fulde, P. & Shtengel, K. Kinetic ferromagnetism on a kagome lattice. *Phys. Rev. Lett.* **100**, 136404 (2008).
59. Johnston, R. L. & Hoffmann, R. The kagomé net: band theoretical and topological aspects. *Polyhedron* **9**, 1901–1911 (1990).
60. Sil, A. & Ghosh, A. K. First and second order topological phases on ferromagnetic breathing kagome lattice. *J. Phys. Condens. Matter* **32**, 205601 (2020).
61. Zhou, H. et al. Orbital degree of freedom induced multiple sets of second-order topological states in two-dimensional breathing kagome crystals. *NPJ Quantum Mater.* **8**, 16 (2023).
62. Lu, X., Chen, Y. & Chen, H. Orbital corner states on breathing kagome lattices. *Phys. Rev. B* **101**, 195143 (2020).
63. Ezawa, M. Higher-order topological insulators and semimetals on the breathing kagome and pyrochlore lattices. *Phys. Rev. Lett.* **120**, 026801 (2018).
64. Herrera, M. A. J. et al. Corner modes of the breathing kagome lattice: origin and robustness. *Phys. Rev. B* **105**, 085411 (2022).
65. Li, M. et al. Higher-order topological states in photonic kagome crystals with long-range interactions. *Nat. Photon.* **14**, 89–94 (2020).
66. El Hassan, A. et al. Corner states of light in photonic waveguides. *Nat. Photon.* **13**, 697–700 (2019).
67. Xue, H., Yang, Y., Gao, F., Chong, Y. & Zhang, B. Acoustic higher-order topological insulator on a kagome lattice. *Nat. Mater.* **18**, 108–112 (2019).
68. Schaffer, R., Huh, Y., Hwang, K. & Kim, Y. B. Quantum spin liquid in a breathing kagome lattice. *Phys. Rev. B* **95**, 054410 (2017).
69. Akbari-Sharbaf, A. et al. Tunable quantum spin liquidity in the 1/6th-filled breathing kagome lattice. *Phys. Rev. Lett.* **120**, 227201 (2018).
70. Kuroda, K. et al. Evidence for magnetic Weyl fermions in a correlated metal. *Nat. Mater.* **16**, 1090–1095 (2017).
71. Armitage, N. P., Mele, E. J. & Vishwanath, A. Weyl and Dirac semimetals in three-dimensional solids. *Rev. Mod. Phys.* **90**, 015001 (2018).
72. Liu, G., Zhang, P., Wang, Z. & Li, S. S. Spin Hall effect on the kagome lattice with Rashba spin–orbit interaction. *Phys. Rev. B* **79**, 035323 (2009).
73. Jones, D. C. et al. Origin of spin reorientation and intrinsic anomalous Hall effect in the kagome ferrimagnet $TbMn_6Sn_6$. Preprint at https://doi.org/10.48550/arXiv.2203.17246 (2022).
74. Asaba, T. et al. Anomalous Hall effect in the kagome ferrimagnet $GdMn_6Sn_6$. *Phys. Rev. B* **101**, 174415 (2020).
75. Liu, E. et al. Giant anomalous Hall effect in a ferromagnetic kagome-lattice semimetal. *Nat. Phys.* **14**, 1125–1131 (2018).
76. Wang, Q. et al. Large intrinsic anomalous Hall effect in half-metallic ferromagnet $Co_3Sn_2S_2$ with magnetic Weyl fermions. *Nat. Commun.* **9**, 3681 (2018).
77. Chen, D. et al. Large anomalous Hall effect in the kagome ferromagnet $LiMn_6Sn_6$. *Phys. Rev. B* **103**, 144410 (2021).
78. Bruno, P., Dugaev, V. K. & Taillefumier, M. Topological Hall effect and Berry phase in magnetic napostructures. *Phys. Rev. Lett.* **93**, 096806 (2004).
79. He, Y. et al. Topological Hall effect arising from the mesoscopic and microscopic non-coplanar magnetic structure in MnBi. *Acta Mater.* **226**, 117619 (2022).
80. Rout, P. K., Madduri, P. V. P., Manna, S. K. & Nayak, A. K. Field-induced topological Hall effect in the noncoplanar triangular antiferromagnetic geometry of Mn_3Sn. *Phys. Rev. B* **99**, 094430 (2019).
81. Taylor, J. M. et al. Anomalous and topological Hall effects in epitaxial thin films of the noncollinear antiferromagnet Mn_3Sn. *Phys. Rev. B* **101**, 094404 (2020).
82. Du, Q. et al. Topological Hall effect anisotropy in kagome bilayer metal Fe_3Sn_2. *Phys. Rev. Lett.* **129**, 236601 (2022).
83. Chakrabarty, D., Jamaluddin, S., Manna, S. K. & Nayak, A. K. Tunable room temperature magnetic skyrmions in centrosymmetric kagome magnet Mn_4Ga_2Sn. *Commun. Phys.* **5**, 189 (2022).
84. Wang, Q. et al. Field-induced topological Hall effect and double-fan spin structure with a c-axis component in the metallic kagome antiferromagnetic compound YMn_6Sn_6. *Phys. Rev. B* **103**, 014416 (2021).
85. Wang, B. et al. Magnetotransport properties of the kagome magnet $TmMn_6Sn_6$. *Phys. Rev. B* **106**, 125107 (2022).
86. Neupert, T., Santos, L., Chamon, C. & Mudry, C. Fractional quantum Hall states at zero magnetic field. *Phys. Rev. Lett.* **106**, 236804 (2011).
87. Ohgushi, K., Murakami, S. & Nagaosa, N. Spin anisotropy and quantum Hall effect in the kagomé lattice: chiral spin state based on a ferromagnet. *Phys. Rev. B* **62**, R6065(R) (2000).
88. Yang, S., Gu, Z. C., Sun, K. & Das Sarma, S. Topological flat band models with arbitrary Chern numbers. *Phys. Rev. B* **86**, 241112(R) (2012).
89. Li, Z. et al. Realization of flat band with possible nontrivial topology in electronic kagome lattice. *Sci. Adv.* **4**, eaau4511 (2018).
90. Chen, Y. et al. Ferromagnetism and Wigner crystallization in kagome graphene and related structures. *Phys. Rev. B* **98**, 035135 (2018).
91. Wu, C., Bergman, D., Balents, L. & Das Sarma, S. Flat bands and Wigner crystallization in the honeycomb optical lattice. *Phys. Rev. Lett.* **99**, 070401 (2007).
92. Jaworowski, B. et al. Wigner crystallization in topological flat bands. *N. J. Phys.* **20**, 063023 (2018).
93. Hu, J. et al. Correlated flat bands and quantum spin liquid state in a cluster Mott insulator. *Commun. Phys.* **6**, 172 (2023).
94. Iglovikov, V. I., Hébert, F., Grémaud, B., Batrouni, G. G. & Scalettar, R. T. Superconducting transitions in flat-band systems. *Phys. Rev. B* **90**, 094506 (2014).
95. Lee, P. A., Nagaosa, N. & Wen, X. G. Doping a Mott insulator: physics of high-temperature superconductivity. *Rev. Mod. Phys.* **78**, 17–85 (2006).
96. Po, H. C., Zou, L., Vishwanath, A. & Senthil, T. Origin of Mott insulating behavior and superconductivity in twisted bilayer graphene. *Phys. Rev. X* **8**, 031089 (2018).
97. Cao, Y. et al. Unconventional superconductivity in magic-angle graphene superlattices. *Nature* **556**, 43–50 (2018).
98. Xu, Y. et al. Electronic correlations and flattened band in magnetic Weyl semimetal candidate $Co_3Sn_2S_2$. *Nat. Commun.* **11**, 3985 (2020).
99. Li, M. et al. Dirac cone, flat band and saddle point in kagome magnet YMn_6Sn_6. *Nat. Commun.* **12**, 3129 (2021).
100. Yang, T. Y. et al. Fermi-level flat band in a kagome magnet. *Quantum Frontiers* **1**, 14 (2022).
101. Kang, M. et al. Twofold van Hove singularity and origin of charge order in topological kagome superconductor CsV_3Sb_5. *Nat. Phys.* **18**, 301–308 (2022).
102. Lee, S. et al. Nature of charge density wave in kagome metal ScV_6Sn_6. Preprint at https://doi.org/10.48550/arXiv.2304.11820 (2023).
103. Yu, S. L. & Li, J. X. Chiral superconducting phase and chiral spin-density-wave phase in a Hubbard model on the kagome lattice. *Phys. Rev. B* **85**, 144402 (2012).
104. Yuan, N. F. Q., Isobe, H. & Fu, L. Magic of high-order van Hove singularity. *Nat. Commun.* **10**, 5769 (2019).
105. Guerci, D., Simon, P. & Mora, C. Higher-order van Hove singularity in magic-angle twisted trilayer graphene. *Phys. Rev. Res.* **4**, L012013 (2022).
106. Classen, L., Chubukov, A. V., Honerkamp, C. & Scherer, M. M. Competing orders at higher-order van Hove points. *Phys. Rev. B* **102**, 125141 (2020).

107. Hu, Y. et al. Rich nature of van Hove singularities in kagome superconductor CsV_3Sb_5. *Nat. Commun.* **13**, 2220 (2022).
108. Jovanovic, M. & Schoop, L. M. Simple chemical rules for predicting band structures of kagome materials. *J. Am. Chem. Soc.* **144**, 10978–10991 (2022).
109. Hoffmann, R. *Solids and Surfaces: A Chemist's View of Bonding in Solids and Surfaces* (VCH, 1988).
110. Hu, Y. et al. Topological surface states and flat bands in the kagome superconductor CsV_3Sb_5. *Sci. Bull.* **67**, 495–500 (2022).
111. Nakayama, K. et al. Multiple energy scales and anisotropic energy gap in the charge-density-wave phase of the kagome superconductor CsV_3Sb_5. *Phys. Rev. B* **104**, L161112 (2021).
112. Wang, N. N. et al. Competition between charge-density-wave and superconductivity in the kagome metal RbV_3Sb_5. *Phys. Rev. Res.* **3**, 043018 (2021).
113. Mu, C. et al. *S*-wave superconductivity in kagome metal CsV_3Sb_5 revealed by $^{121/123}$Sb NQR and ^{51}V NMR measurements. *Chin. Phys. Lett.* **38**, 077402 (2021).
114. Luo, J. et al. Possible Star-of-David pattern charge density wave with additional modulation in the kagome superconductor CsV_3Sb_5. *NPJ Quantum Mater.* **7**, 30 (2022).
115. Song, D. et al. Orbital ordering and fluctuations in a kagome superconductor CsV_3Sb_5. *Sci. China* **65**, 247462 (2022).
116. Jiang, Y. X. et al. Unconventional chiral charge order in kagome superconductor KV_3Sb_5. *Nat. Mater.* **20**, 1353–1357 (2021).
117. Li, H. et al. Rotation symmetry breaking in the normal state of a kagome superconductor KV_3Sb_5. *Nat. Phys.* **18**, 265–270 (2022).
118. Shumiya, N. et al. Intrinsic nature of chiral charge order in the kagome superconductor RbV_3Sb_5. *Phys. Rev. B* **104**, 035131 (2021).
119. Wang, Z. et al. Electronic nature of chiral charge order in the kagome superconductor CsV_3Sb_5. *Phys. Rev. B* **104**, 075148 (2021).
120. Nie, L. et al. Charge-density-wave-driven electronic nematicity in a kagome superconductor. *Nature* **604**, 59–64 (2022).
121. Li, H. et al. Unidirectional coherent quasiparticles in the high-temperature rotational symmetry broken phase of AV_3Sb_5 kagome superconductors. *Nat. Phys.* **19**, 637–643 (2023).
122. Wang, Q. et al. Charge density wave orders and enhanced superconductivity under pressure in the kagome metal CsV_3Sb_5. *Adv. Mater.* **33**, 2102813 (2021).
123. Yu, J. et al. Evolution of electronic structure in pristine and Rb-reconstructed surfaces of kagome metal RbV_3Sb_5. *Nano Lett.* **22**, 918–925 (2022).
124. Liang, Z. et al. Three-dimensional charge density wave and surface-dependent vortex-core states in a kagome superconductor CsV_3Sb_5. *Phys. Rev. X* **11**, 031026 (2021).
125. Kato, T. et al. Surface-termination-dependent electronic states in kagome superconductors AV_3Sb_5 (A=K, Rb, Cs) studied by micro-ARPES. *Phys. Rev. B* **107**, 245143 (2023).
126. Kato, T. et al. Polarity-dependent charge density wave in the kagome superconductor CsV_3Sb_5. *Phys. Rev. B* **106**, L121112 (2022).
127. Li, H. et al. Small Fermi pockets intertwined with charge stripes and pair density wave order in a kagome superconductor. Preprint at https://doi.org/10.48550/arXiv.2303.07254 (2023).
128. Ye, Z., Luo, A., Yin, J. X., Hasan, M. Z. & Xu, G. Structural instability and charge modulations in the kagome superconductor AV_3Sb_5. *Phys. Rev. B* **105**, 245121 (2022).
129. Xiang, Y. et al. Twofold symmetry of c-axis resistivity in topological kagome superconductor CsV_3Sb_5 with in-plane rotating magnetic field. *Nat. Commun.* **12**, 6727 (2021).
130. Xu, Y. et al. Three-state nematicity and magneto-optical Kerr effect in the charge density waves in kagome superconductors. *Nat. Phys.* **18**, 1470–1475 (2022).
131. Wu, Q. et al. Simultaneous formation of two-fold rotation symmetry with charge order in the kagome superconductor CsV_3Sb_5 by optical polarization rotation measurement. *Phys. Rev. B* **106**, 205109 (2022).
132. Jiang, Z. et al. Observation of electronic nematicity driven by three-dimensional charge density wave in kagome lattice KV_3Sb_5. *Nano Lett.***23**, 5625–5633 (2023).
133. Wulferding, D. et al. Emergent nematicity and intrinsic versus extrinsic electronic scattering processes in the kagome metal CsV_3Sb_5. *Phys. Rev. Res.* **4**, 023215 (2022).
134. Miao, H. et al. Geometry of the charge density wave in the kagome metal AV_3Sb_5. *Phys. Rev. B* **104**, 195132 (2021).
135. Park, T., Ye, M. & Balents, L. Electronic instabilities of kagome metals: saddle points and Landau theory. *Phys. Rev. B* **104**, 035142 (2021).
136. Li, H. et al. Observation of unconventional charge density wave without acoustic phonon anomaly in kagome superconductors AV_3Sb_5 (A=Rb, Cs). *Phys. Rev. X* **11**, 031050 (2021).
137. Ratcliff, N., Hallett, L., Ortiz, B. R., Wilson, S. D. & Harter, J. W. Coherent phonon spectroscopy and interlayer modulation of charge density wave order in the kagome metal CsV_3Sb_5. *Phys. Rev. Mater.* **5**, L111801 (2021).
138. Stahl, Q. et al. Temperature-driven reorganization of electronic order in CsV_3Sb_5. *Phys. Rev. B* **105**, 195136 (2022).
139. Ortiz, B. R. et al. Fermi surface mapping and the nature of charge-density-wave order in the kagome superconductor CsV_3Sb_5. *Phys. Rev. X* **11**, 041030 (2021).
140. Kautzsch, L. et al. Structural evolution of the kagome superconductors AV_3Sb_5 (A=K, Rb, and Cs) through charge density wave order. *Phys. Rev. Mater.* **7**, 024806 (2023).
141. Li, H. et al. Discovery of conjoined charge density waves in the kagome superconductor CsV_3Sb_5. *Nat. Commun.* **13**, 6348 (2022).
142. Xiao, Q. et al. Coexistence of multiple stacking charge density waves in kagome superconductor CsV_3Sb_5. *Phys. Rev. Res.* **5**, L012032 (2023).
143. Wu, S. et al. Charge density wave order in the kagome metal AV_3Sb_5 (A=Cs,Rb, K). *Phys. Rev. B* **105**, 155106 (2022).
144. Wang, Z. X. et al. Unconventional charge density wave and photoinduced lattice symmetry change in the kagome metal CsV_3Sb_5 probed by time-resolved spectroscopy. *Phys. Rev. B* **104**, 165110 (2021).
145. Johannes, M. D. & Mazin, I. I. Fermi surface nesting and the origin of charge density waves in metals. *Phys. Rev. B* **77**, 165135 (2008).
146. Varma, C. M. & Simons, A. L. Strong-coupling theory of charge-density-wave transitions. *Phys. Rev. Lett.* **51**, 138–141 (1983).
147. Kang, M. et al. Charge order landscape and competition with superconductivity in kagome metals. *Nat. Mater.* **22**, 186–193 (2023).
148. Luo, Y. et al. Electronic states dressed by an out-of-plane supermodulation in the quasi-two-dimensional kagome superconductor CsV_3Sb_5. *Phys. Rev. B* **105**, L241111 (2022).
149. Lou, R. et al. Charge-density-wave-induced peak–dip–hump structure and the multiband superconductivity in a kagome superconductor CsV_3Sb_5. *Phys. Rev. Lett.* **128**, 036402 (2022).
150. Wang, Z. et al. Distinctive momentum dependent charge-density-wave gap observed in CsV_3Sb_5 superconductor with topological kagome lattice. Preprint at https://doi.org/10.48550/arXiv.2104.05556 (2021).
151. Liu, Z. et al. Charge-density-wave-induced bands renormalization and energy gaps in a kagome superconductor RbV_3Sb_5. *Phys. Rev. X* **11**, 041010 (2021).
152. Kato, T. et al. Three-dimensional energy gap and origin of charge-density wave in kagome superconductor KV_3Sb_5. *Commun. Mater.* **3**, 30 (2022).
153. Uykur, E. et al. Low-energy optical properties of the nonmagnetic kagome metal. *Phys. Rev. B* **104**, 045130 (2021).
154. Zhou, X. et al. Origin of charge density wave in the kagome metal CsV_3Sb_5 as revealed by optical spectroscopy. *Phys. Rev. B* **104**, L041101 (2021).
155. Liu, G. et al. Observation of anomalous amplitude modes in the kagome metal CsV_3Sb_5. *Nat. Commun.* **13**, 3461 (2022).
156. Luo, H. et al. Electronic nature of charge density wave and electron-phonon coupling in kagome superconductor KV_3Sb_5. *Nat. Commun.* **13**, 273 (2022).
157. Uykur, E., Ortiz, B. R., Wilson, S. D., Dressel, M. & Tsirlin, A. A. Optical detection of the density-wave instability in the kagome metal KV_3Sb_5. *NPJ Quantum Mater.* **7**, 16 (2022).
158. Xie, Y. et al. Electron-phonon coupling in the charge density wave state of CsV_3Sb_5. *Phys. Rev. B* **105**, L140501 (2022).
159. Christensen, M. H., Birol, T., Andersen, B. M. & Fernandes, R. M. Theory of the charge density wave in AV_3Sb_5 kagome metals. *Phys. Rev. B* **104**, 214513 (2021).
160. Tan, H., Liu, Y., Wang, Z. & Yan, B. Charge density waves and electronic properties of superconducting kagome metals. *Phys. Rev. Lett.* **127**, 046401 (2021).
161. Grandi, F., Consiglio, A., Sentef, M. A., Thomale, R. & Kennes, D. M. Theory of nematic charge orders in kagome metals. *Phys. Rev. B* **107**, 155131 (2023).
162. Feng, X., Zhang, Y., Jiang, K. & Hu, J. Low-energy effective theory and symmetry classification of flux phases on the kagome lattice. *Phys. Rev. B* **104**, 165136 (2021).
163. Lin, Y. P. & Nandkishore, R. M. Complex charge density waves at van Hove singularity on hexagonal lattices: Haldane-model phase diagram and potential realization in the kagome metals AV_3Sb_5 (=K, Rb, Cs). *Phys. Rev. B* **104**, 045122 (2021).
164. Christensen, M. H., Birol, T., Andersen, B. M. & Fernandes, R. M. Loop currents in AV_3Sb_5 kagome metals: multipolar and toroidal magnetic orders. *Phys. Rev. B* **106**, 144504 (2022).
165. Mu, C. et al. Tri-hexagonal charge order in kagome metal CsV_3Sb_5 revealed by ^{121}Sb nuclear quadrupole resonance. *Chin. Phys. B* **31**, 017105 (2022).
166. Frassineti, J. et al. Microscopic nature of the charge-density wave in kagome superconductor RbV_3Sb_5. *Phys. Rev. Res.* **5**, L012017 (2023).
167. Wang, Y., Wu, T., Li, Z., Jiang, K. & Hu, J. Structure of kagome superconductor CsV_3Sb_5 in the charge density wave states. *Phys. Rev. B* **107**, 184106 (2023).
168. Hu, Y. et al. Coexistence of trihexagonal and star-of-David pattern in the charge density wave of the kagome superconductor AV_3Sb_5. *Phys. Rev. B* **106**, L241106 (2022).
169. Broyles, C., Graf, D., Yang, H., Gao, H. & Ran, S. Effect of the interlayer ordering on the Fermi surface of kagome superconductor CsV_3Sb_5 revealed by quantum oscillations. *Phys. Rev. Lett.* **129**, 157001 (2022).
170. Kautzsch, L. et al. Incommensurate charge-stripe correlations in the kagome superconductor $CsV_3Sb_{5-x}Sn_x$. *NPJ Quantum Mater.* **8**, 37 (2023).
171. Kenney, E. M., Ortiz, B. R., Wang, C., Wilson, S. D. & Graf, M. J. Absence of local moments in the kagome metal KV_3Sb_5 as determined by muon spin spectroscopy. *J. Phys. Condens. Matter* **33**, 235801 (2021).
172. Li, H. et al. No observation of chiral flux current in the topological kagome metal CsV_3Sb_5. *Phys. Rev. B* **105**, 045102 (2022).
173. Saykin, D. R. et al. High resolution polar Kerr effect studies of CsV_3Sb_5: tests for time-reversal symmetry breaking below the charge-order transition. *Phys. Rev. Lett.* **131**, 016901 (2023).
174. Yu, L. et al. Evidence of a hidden flux phase in the topological kagome metal CsV_3Sb_5. Preprint at https://doi.org/10.48550/arXiv.2107.10714 (2021).
175. Mielke, C. et al. Time-reversal symmetry-breaking charge order in a kagome superconductor. *Nature* **602**, 245–250 (2022).
176. Khasanov, R. et al. Time-reversal symmetry broken by charge order in CsV_3Sb_5. *Phys. Rev. Res.* **4**, 023244 (2022).
177. Chen, D. et al. Anomalous thermoelectric effects and quantum oscillations in the kagome metal CsV_3Sb_5. *Phys. Rev. B* **105**, L201109 (2022).

178. Mi, X. et al. Multiband effects in thermoelectric and electrical transport properties of kagome superconductors AV_3Sb_5 (A=K, Rb, Cs). *New J. Phys.* **24**, 093021 (2022).
179. Zhou, X. et al. Anomalous thermal Hall effect and anomalous nernst effect of CsV_3Sb_5. *Phys. Rev. B* **105**, 205104 (2022).
180. Hu, Y. et al. Time-reversal symmetry breaking in charge density wave of CsV_3Sb_5 detected by polar Kerr effect. Preprint at *Research Square* https://doi.org/10.21203/rs.3.rs-1794207/v1 (2022).
181. Feng, X., Jiang, K., Wang, Z. & Hu, J. Chiral flux phase in the kagome superconductor AV_3Sb_5. *Sci. Bull.* **66**, 1384–1388 (2021).
182. Denner, M. M., Thomale, R. & Neupert, T. Analysis of charge order in the kagome metal AV_3Sb_5(A=K; Rb; Cs). *Phys. Rev. Lett.* **127**, 217601 (2021).
183. Dong, J. W., Wang, Z. & Zhou, S. Loop-current charge density wave driven by long-range Coulomb repulsion on the kagomé lattice. *Phys. Rev. B* **107**, 045127 (2023).
184. Guo, C. et al. Switchable chiral transport in charge-ordered kagome metal CsV_3Sb_5. *Nature* **611**, 461–466 (2022).
185. Scammell, H. D., Ingham, J., Li, T. & Sushkov, O. P. Chiral excitonic order from twofold van Hove singularities in kagome metals. *Nat. Commun.* **14**, 605 (2023).
186. Xu, H. et al. Multiband superconductivity with sign-preserving order parameter in kagome superconductor CsV_3Sb_5. *Phys. Rev. Lett.* **127**, 187004 (2021).
187. Gupta, R. et al. Microscopic evidence for anisotropic multigap superconductivity in the CsV_3Sb_5 kagome superconductor. *NPJ Quantum Mater.* **7**, 49 (2022).
188. Duan, W. et al. Nodeless superconductivity in the kagome metal CsV_3Sb_5. *Sci. China Phys. Mech. Astron.* **64**, 107462 (2021).
189. Roppongi, M. et al. Bulk evidence of anisotropic *s*-wave pairing with no sign change in the kagome superconductor CsV_3Sb_5. *Nat. Commun.* **14**, 667 (2023).
190. Deng, J., Zhang, R., Xie, Y., Wu, X. & Wang, Z. Fermi surface nesting and surface topological superconductivity in AV_3Sb_5. Preprint at https://doi.org/10.48550/arXiv.2302.06211 (2023).
191. Jiang, H. M., Liu, M. X. & Yu, S. L. Impact of the orbital current order on the superconducting properties of the kagome superconductors. *Phys. Rev. B* **107**, 064506 (2023).
192. Gu, Y., Zhang, Y., Feng, X., Jiang, K. & Hu, J. Gapless excitations inside the fully gapped kagome superconductors AV_3Sb_5. *Phys. Rev. B* **105**, L100502 (2022).
193. Zhao, C. C. et al. Nodal superconductivity and superconducting domes in the topological. Preprint at https://doi.org/10.48550/arXiv.2102.08356 (2021).
194. Guguchia, Z. et al. Tunable unconventional kagome superconductivity in charge ordered RbV_3Sb_5 and KV_3Sb_5. *Nat. Commun.* **14**, 153 (2023).
195. Shan, Z. et al. Muon spin relaxation study of the layered kagome superconductor CsV_3Sb_5. *Phys. Rev. Res.* **4**, 033145 (2022).
196. Gupta, R. et al. Two types of charge order with distinct interplay with superconductivity in the kagome material CsV_3Sb_5. *Commun. Phys.* **5**, 232 (2022).
197. Zheng, L. et al. Emergent charge order in pressurized kagome superconductor CsV_3Sb_5. *Nature* **611**, 682–687 (2022).
198. Wang, Y. et al. Anisotropic proximity-induced superconductivity and edge supercurrent in kagome metal, $K_{1-x}V_3Sb_5$. *Sci. Adv.* **9**, eadg7269 (2023).
199. Zhao, J., Wu, W., Wang, Y. & Yang, S. A. Electronic correlations in the normal state of the kagome superconductor KV_3Sb_5. *Phys. Rev. B* **103**, L241117 (2021).
200. Wu, X. et al. Nature of unconventional pairing in the kagome superconductors. *Phys. Rev. Lett.* **127**, 177001 (2021).
201. Rømer, A. T., Bhattacharyya, S., Valentí, R., Christensen, M. H. & Andersen, B. M. Superconductivity from repulsive interactions on the kagome lattice. *Phys. Rev. B* **106**, 174514 (2022).
202. Tazai, R., Yamakawa, Y., Onari, S. & Kontani, H. Mechanism of exotic density-wave and beyond-Migdal unconventional superconductivity in kagome metal AV_3Sb_5 (A=K, Rb, Cs). *Sci. Adv.* **8**, eabl4108 (2022).
203. Herland, E. V., Babaev, E. & Sudbø, A. Phase transitions in a three dimensional U(1)×u(1) lattice London superconductor: metallic superfluid and charge-4e superconducting states. *Phys. Rev. B* **82**, 134511 (2010).
204. Zhou, S. & Wang, Z. Chern Fermi pocket, topological pair density wave, and charge-4e and charge-6e superconductivity in kagomé superconductors. *Nat. Commun.* **13**, 7288 (2022).
205. Agterberg, D. F., Geracie, M. & Tsunetsugu, H. Conventional and charge-six superfluids from melting hexagonal Fulde-Ferrell-Larkin-Ovchinnikov phases in two dimensions. *Phys. Rev. B* **84**, 014513 (2011).
206. Berg, E., Fradkin, E. & Kivelson, S. A. Charge-4e superconductivity from pair-density-wave order in certain high-temperature superconductors. *Nat. Phys.* **5**, 830–833 (2009).
207. Jian, S., Huang, Y. & Yao, H. Charge-4e superconductivity from nematic superconductors in two and three dimensions. *Phys. Rev. Lett.* **127**, 227001 (2021).
208. Ge, J. et al. Discovery of charge-4e and charge-6e superconductivity in kagome superconductor CsV_3Sb_5. Preprint at https://doi.org/10.48550/arXiv.2201.10352 (2022).
209. Han, J. H. & Lee, P. A. Understanding resistance oscillation in the CsV_3Sb_5 superconductor. *Phys. Rev. B* **106**, 184515 (2022).
210. Yu, Y. Non-uniform vestigial charge-4e phase in the kagome superconductor CsV_3Sb_5. Preprint at https://doi.org/10.48550/arXiv.2210.00023 (2022).
211. Du, F. et al. Pressure-induced double superconducting domes and charge instability in the kagome metal KV_3Sb_5. *Phys. Rev. B* **103**, L220504 (2021).
212. Chen, K. Y. et al. Double superconducting dome and triple enhancement of T_c in the kagome superconductor CsV_3Sb_5. *Phys. Rev. Lett.* **126**, 247001 (2021).
213. Yu, F. H. et al. Unusual competition of superconductivity and charge-density-wave state in a compressed topological kagome metal. *Nat. Commun.* **12**, 3645 (2021).
214. Li, Y. et al. Tuning the competition between superconductivity and charge order in the kagome superconductor $Cs(V_{1-x}Nb_x)_3Sb_5$. *Phys. Rev. B* **105**, L180507 (2022).
215. Nakayama, K. et al. Carrier injection and manipulation of charge-density wave in kagome superconductor. *Phys. Rev. X* **12**, 011001 (2022).
216. Yin, L. et al. Strain-sensitive superconductivity in the kagome metals KV_3Sb_5 and CsV_3Sb_5 probed by point-contact spectroscopy. *Phys. Rev. B* **104**, 174507 (2021).
217. Consiglio, A. et al. Van Hove tuning of AV_3Sb_5 kagome metals under pressure and strain. *Phys. Rev. B* **105**, 165146 (2022).
218. Zhu, C. C. et al. Double-dome superconductivity under pressure in the V-based kagome metals AV_3Sb_5 (A=Rb and K). *Phys. Rev. B* **105**, 094507 (2022).
219. Zhang, Z. et al. Pressure-induced reemergence of superconductivity in the topological kagome metal CsV_3Sb_5. *Phys. Rev. B* **103**, 224513 (2021).
220. Chen, X. et al. Highly robust reentrant superconductivity in CsV_3Sb_5 under pressure. *Chin. Phys. Lett.* **38**, 057402 (2021).
221. Tsirlin, A. A. et al. Role of Sb in the superconducting kagome metal CsV_3Sb_5 revealed by its anisotropic compression. *SciPost Phys.* **12**, 049 (2022).
222. Labollita, H. & Botana, A. S. Tuning the van Hove singularities in AV_3Sb_5 (A=K, Rb, Cs) via pressure and doping. *Phys. Rev. B* **104**, 205129 (2021).
223. Kato, T. et al. Fermiology and origin of T_c enhancement in a kagome superconductor $Cs(V_{1-x}Nb_x)_3Sb_5$. *Phys. Rev. Lett.* **129**, 206402 (2022).
224. Liu, Y. et al. Doping evolution of superconductivity, charge order and band topology in hole-doped topological kagome superconductors $Cs(V_{1-x}Ti_x)_3Sb_5$. *Phys. Rev. Mater.* **7**, 064801 (2023).
225. Oey, Y. M., Kaboudvand, F., Ortiz, B. R., Seshadri, R. & Wilson, S. D. Tuning charge density wave order and superconductivity in the kagome metals $KV_3Sb_{5-x}Sn_x$ and $RbV_3Sb_{5-x}Sn_x$. *Phys. Rev. Mater.* **6**, 074802 (2022).
226. Oey, Y. M. et al. Fermi level tuning and double-dome superconductivity in the kagome metal $CsV_3Sb_{5-x}Sn_x$. *Phys. Rev. Mater.* **6**, L041801 (2022).
227. Song, Y. et al. Competition of superconductivity and charge density wave in selective oxidized CsV_3Sb_5 thin flakes. *Phys. Rev. Lett.* **127**, 237001 (2021).
228. Zhang, W. et al. Emergence of large quantum oscillation frequencies in thin flakes of a kagome superconductor CsV_3Sb_5. *Phys. Rev. B* **106**, 195103 (2022).
229. Song, B. et al. Anomalous enhancement of charge density wave in kagome superconductor CsV_3Sb_5 approaching the 2D limit. *Nat. Commun.* **14**, 2492 (2023).
230. Zheng, G. et al. Electrically controlled superconductor-to-failed insulator transition and giant anomalous Hall effect in kagome metal CsV_3Sb_5 nanoflakes. *Nat. Commun.* **14**, 678 (2023).
231. Kim, S.-W., Oh, H., Moon, E.-G. & Kim, Y. Monolayer kagome metals AV_3Sb_5. *Nat. Commun.* **14**, 591 (2023).
232. Casola, F., Van Der Sar, T. & Yacoby, A. Probing condensed matter physics with magnetometry based on nitrogen-vacancy centres in diamond. *Nat. Rev. Mater.* **3**, 17088 (2018).
233. Vasyukov, D. et al. A scanning superconducting quantum interferometer device with single electron spin sensitivity. *Nat. Nanotechnol.* **8**, 639–644 (2013).
234. Spinelli, A., Bryant, B., Delgado, F., Fernández-Rossier, J. & Otte, A. F. Imaging of spin waves in atomically designed nanomagnets. *Nat. Mater.* **13**, 782–785 (2014).
235. Olenych, R. R., Akselrud, L. G. & Yarmolyuk, Y. P. Crystal structure of ternary germanides RFe_6Ge_6 (R=Sc, Ti, Zr, Hf, Nb) and RCo_6Ge_6 (R=Ti, Zr, Hf). *Dopov. Akad. Nauk. Ukr. RSR Ser. A* **2**, 84–88 (1981).
236. Buchholz, W. & Schuster, H.-U. Intermetallische Phasen mit b35-uberstruktur und verwandtschaftsbeziehung zu $LiFe_6Ge_6$. *Z. Anorg. Allg. Chem.* **48**, 40–48 (1981).
237. Rao, X.-L.& Coey, J. M. D. Mössbauer study of the magnetic properties of RFe_6Sn_6 compounds (R=Y, Gd, Tb, Dy, Ho, Er, Tm). *J. Appl. Phys.* **81**, 5181–5183 (1997).
238. Venturini, G., Welter, R. & Malaman, B. Crystallographic data and magnetic properties of RT_6Ge_6 compounds (R Sc, Y, Nd, Sm, GdLu; TMn, Fe). *J. Alloy. Compd.* **185**, 99–107 (1992).
239. El Idrissi, B. C., Venturini, G. & Malaman, B. Crystal structures of RFe_6Sn_6 (R=Sc, Y, Gd Tm, Lu) rare-earth iron stannides. *Mater. Res. Bull.* **26**, 1331–1338 (1991).
240. Idrissi, B. C. E., Venturini, G., Malaman, B. & Ressouche, E. Magnetic properties of $NdMn_6Ge_6$ and $SmMn_6Ge_6$ compounds from susceptibility. *J. Alloys Compd.* **215**, 187–193 (1994).
241. Gao, L. et al. Anomalous Hall effect in ferrimagnetic metal RMn_6Sn_6(R=Tb, Dy, Ho) with clean Mn kagome lattice. *Appl. Phys. Lett.* **119**, 092405 (2021).
242. Avila, M. A., Takabatake, T., Takahashi, Y., Bud'ko, S. L. & Canfield, P. C. Direct observation of Fe spin reorientation in single-crystalline $YbFe_6Ge_6$. *J. Phys. Condens. Matter* **17**, 6969–6979 (2005).
243. Duijn, H. G. M., Brück, E., Buschow, K. H. J. & De Beer, F. R. Electrical resistivity of RMn_6Ge_6 (R=rare earth) compounds. *J. Magn. Magn. Mater.* **196**, 691–693 (1999).
244. Malaman, B. et al. Magnetic properties of RMn_6Sn_6 (R=Gd-Er) compounds from neutron diffraction and Mossbauer measurements. *J. Magn. Magn. Mater.* **202**, 519–534 (1999).
245. Clatterbuck, D. M. & Gschneidner Jr, K. A. Magnetic properties of RMn_6Sn_6 (R=Tb, Ho, Er, Tm, Lu) single crystals. *J. Magn. Magn. Mater.* **207**, 78–94 (1999).
246. Venturini, G., Idrissi, B. C., El & Malaman, B. Magnetic properties of RMn_6Sn_6 (R=Sc, Y, Gd-Tm, Lu) compounds with $HfFe_6Ge_6$ type structure. *J. Magn. Magn. Mater.* **94**, 35–42 (1991).
247. Lee, Y. et al. Interplay between magnetism and band topology in Kagome magnets RMn_6Sn_6. *Phys. Rev. B* **108**, 045132 (2023).
248. Mielke, C. et al. Low-temperature magnetic crossover in the topological kagome magnet $TbMn_6Sn_6$. *Commun. Phys.* **5**, 107 (2022).

249. Venturini, G., Fruchart, D. & Malaman, B. Incommensurate magnetic structures of RMn_6Sn_6(R=Sc, Y, Lu) compounds from neutron diffraction study. *J. Alloy. Compd.* **236**, 102–110 (1996).
250. Ghimire, N. J. et al. Competing magnetic phases and fluctuation-driven scalar spin chirality in the kagome metal YMn_6Sn_6. *Sci. Adv.* **6**, eabe2680 (2020).
251. Venturini, G., Welter, R., Malaman, B. & Ressouche, E. Magnetic structure of YMn_6Ge_6 and room temperature magnetic structure of $LuMn_6Sn_6$ obtained from neutron diffraction study. *J. Alloy. Compd.* **200**, 51–57 (1993).
252. Rosenfeld, E. V. & Mushnikov, N. V. Double-flat-spiral magnetic structures: theory and application to the RMn_6X_6 compounds. *Phys. B Condens. Matter* **403**, 1898–1906 (2008).
253. Mulder, F. M., Thiel, R. C., Brabers, J. H. V. J., de Boer, F. R. & Buschow, K. H. J. ^{155}Gd Mössbauer effect and magnetic properties of $GdMn_6Ge_6$. *J. Alloy. Compd.* **190**, L29–L31 (1993).
254. Siegfried, P. E. et al. Magnetization-driven Lifshitz transition and charge–spin coupling in the kagome metal YMn_6Sn_6. *Commun. Phys.* **5**, 58 (2022).
255. Dally, R. L. et al. Chiral properties of the zero-field spiral state and field-induced magnetic phases of the itinerant kagome metal YMn_6Sn_6. *Phys. Rev. B* **103**, 094413 (2021).
256. Mazet, T., Ihou-Mouko, H., Marêché, J. F. & Malaman, B. Magnetic properties and ^{119}Sn hyperfine interaction parameters of $LiMn_6Sn_6$. *Eur. Phys. J. B* **51**, 173–180 (2006).
257. Pokharel, G. et al. Electronic properties of the topological kagome metals YV_6Sn_6 and GdV_6Sn_6. *Phys. Rev. B* **104**, 235139 (2021).
258. Arachchige, H. W. S. et al. Charge density wave in kagome lattice intermetallic ScV_6Sn_6. *Phys. Rev. Lett.* **129**, 216402 (2022).
259. Sinha, M. et al. Twisting of 2D kagomé sheets in layered intermetallics. *ACS Cent. Sci.* **7**, 1381–1390 (2021).
260. Weiland, A. et al. Refine intervention: characterizing disordered $Yb_{0.5}Co_3Ge_3$. *Cryst. Growth Des.* **20**, 6715–6721 (2020).
261. Wang, Y. et al. Electronic properties and phase transition in the kagome metal $Yb_{0.5}Co_3Ge_3$. *Chem. Mater.* **34**, 7337–7343 (2022).
262. Hu, Y. et al. Tunable topological Dirac surface states and van Hove singularities in kagome metal GdV_6Sn_6. *Sci. Adv.* **8**, eadd2024 (2022).
263. Peng, S. et al. Realizing kagome band structure in two-dimensional kagome surface states of RV_6Sn_6 (R=Gd, Ho). *Phys. Rev. Lett.* **127**, 266401 (2021).
264. Shi, M. et al. A new class of bilayer kagome lattice compounds with Dirac nodal lines and pressure-induced superconductivity. *Nat. Commun.* **13**, 2773 (2022).
265. Yang, Y. et al. Type-II nodal line fermions in the Z_2 topological semimetals AV_6Sb_6 (A=K, Rb, and Cs) with a kagome bilayer. *Phys. Rev. B* **104**, 245128 (2021).
266. Zou, J., He, Z. & Xu, G. The study of magnetic topological semimetals by first principles calculations. *NPJ Comput. Mater.* **5**, 96 (2019).
267. Xu, X. et al. Topological charge-entropy scaling in kagome Chern magnet $TbMn_6Sn_6$. *Nat. Commun.* **13**, 1197 (2022).
268. Min, L. et al. A topological kagome magnet in high entropy form. *Commun. Phys.* **5**, 63 (2022).
269. Kang, S. et al. Emergence of a new band and the Lifshitz transition in kagome metal ScV_6Sn_6 with charge density wave. Preprint at https://doi.org/10.48550/arXiv.2302.14041 (2023).
270. Strempfer, J., Shekhar, C. & Vescovo, E. Softening of a flat phonon mode in the kagome ScV_6Sn_6. Preprint at https://doi.org/10.48550/arXiv.2304.09173 (2023).
271. Cao, S. et al. Competing charge-density wave instabilities in the kagome metal ScV_6Sn_6. Preprint at https://doi.org/10.48550/arXiv.2304.08197 (2023).
272. Hu, Y. et al. Phonon promoted charge density wave in topological kagome metal ScV_6Sn_6. Preprint at https://doi.org/10.48550/arXiv.2304.06431 (2023).
273. Gu, Y. et al. Origin and stability of the charge density wave in ScV_6Sn_6. Preprint at *Research Square* https://doi.org/10.21203/rs.3.rs-2880554/v1 (2023).
274. Cheng, S. et al. Nanoscale visualization and spectral fingerprints of the charge order in ScV_6Sn_6 distinct from other kagome metals. Preprint at https://doi.org/10.48550/arXiv.2302.12227 (2023).
275. Tuniz, M. et al. Dynamics and resilience of the charge density wave in a bilayer kagome metal. Preprint at https://doi.org/10.48550/arXiv.2302.10699 (2023).
276. Hu, T. et al. Optical spectroscopy and band structure calculations of the structural phase transition in the vanadium-based kagome metal ScV_6Sn_6. *Phys. Rev. B* **107**, 165119 (2023).
277. Tan, H. & Yan, B. Abundant lattice instability in kagome metal ScV_6Sn_6. *Phys. Rev. Lett.* **130**, 266402 (2023).
278. Zhang, X. et al. Destabilization of the charge density wave and the absence of superconductivity in ScV_6Sn_6 under high pressures up to 11 GPa. *Materials (Basel)* **15**, 7372 (2022).
279. Guguchia, Z. et al. Hidden magnetism uncovered in charge ordered bilayer kagome material ScV_6Sn_6. Preprint at https://arxiv.org/abs/2304.06436 (2023).
280. Gieck, C., Schreyer, M., Fässler, T. F., Cavet, S. & Claus, P. Synthesis, crystal structure, and catalytic properties of $MgCo_6Ge_6$. *Chem. - A Eur. J.* **12**, 1924–1930 (2006).
281. Kolincio, K. K., Roman, M., Winiarski, M. J., Strychalska-Nowak, J. & Klimczuk, T. Magnetism and charge density waves in $RNiC_2$ (R=Ce, Pr, Nd). *Phys. Rev. B* **95**, 235156 (2017).
282. Lei, H., Wang, K. & Petrovic, C. Magnetic-field-tuned charge density wave in $SmNiC_2$ and $NdNiC_2$. *J. Phys. Condens. Matter* **29**, 075602 (2017).
283. Li, B., Li, S. & Wen, H. H. Chemical doping effect in the $LaRu_3Si_2$ superconductor with a kagome lattice. *Phys. Rev. B* **94**, 094523 (2016).
284. Gui, X. & Cava, R. J. $LaIr_3Ga_2$: a superconductor based on a kagome lattice of Ir. *Chem. Mater.* **34**, 2824–2832 (2022).
285. Gong, C. et al. Superconductivity in kagome metal YRu_3Si_2 with strong electron correlations. *Chin. Phys. Lett.* **39**, 087401 (2022).
286. Mielke, C. et al. Nodeless kagome superconductivity in $LaRu_3Si_2$. *Phys. Rev. Mater.* **5**, 034803 (2021).
287. Kennedy, J. R., Adler, P., Dronskowski, R. & Simon, A. Experimental and theoretical electronic structure investigations on α-Nb_3Cl_8 and the intercalated phase β′-$NaNb_3Cl_8$. *Inorg. Chem.* **35**, 2276–2282 (1996).
288. Kim, B. J. et al. Structural and electrical properties of Nb_3I_8 layered crystal. *Phys. Status Solidi Rapid Res. Lett.* **13**, 1800448 (2019).
289. Haraguchi, Y. et al. Magnetic-nonmagnetic phase transition with interlayer charge disproportionation of Nb_3 trimers in the cluster compound Nb_3Cl_8. *Inorg. Chem.* **56**, 3483–3488 (2017).
290. Sheckelton, J. P., Plumb, K. W., Trump, B. A., Broholm, C. L. & McQueen, T. M. Rearrangement of van der Waals stacking and formation of a singlet state at: T=90 K in a cluster magnet. *Inorg. Chem. Front.* **4**, 481–490 (2017).
291. Conte, F., Ninno, D. & Cantele, G. Layer-dependent electronic and magnetic properties of Nb_3I_8. *Phys. Rev. Res.* **2**, 033001 (2020).
292. Jiang, J. et al. Exploration of new ferromagnetic, semiconducting and biocompatible Nb_3X_8 (X=Cl, Br or I) monolayers with considerable visible and infrared light absorption. *Nanoscale* **9**, 2992–3001 (2017).
293. Grytsiuk, S., Katsnelson, M. I., van Loon, E. G. C. P. & Rösner, M. Nb_3Cl_8: a prototypical layered Mott-Hubbard insulator. Preprint at https://doi.org/10.48550/arXiv.2305.04854 (2023).
294. Sun, Z. et al. Observation of topological flat bands in the kagome semiconductor Nb_3Cl_8. *Nano Lett.* **22**, 4596–4602 (2022).
295. Yoon, J. et al. Anomalous thickness-dependent electrical conductivity in van der Waals layered transition metal halide, Nb_3Cl_8. *J. Phys. Condens. Matter* **32**, 304004 (2020).
296. Xu, Y. et al. Three-dimensional real space invariants, obstructed atomic insulators and a new principle for active catalytic sites. Preprint at https://doi.org/10.48550/arXiv.2111.02433 (2021).
297. Xu, Y. et al. Filling-enforced obstructed atomic insulators. Preprint at https://doi.org/10.48550/arXiv.2106.10276 (2021).
298. Zhang, Y., Gu, Y., Li, P., Hu, J. & Jiang, K. General theory of Josephson diodes. *Phys. Rev. X* **12**, 041013 (2022).
299. Peng, R. et al. Intrinsic anomalous valley Hall effect in single-layer Nb_3I_8. *Phys. Rev. B* **102**, 035412 (2020).
300. Regmi, S. et al. Spectroscopic evidence of flat bands in breathing kagome semiconductor Nb_3I_8. *Commun. Mater.* **3**, 100 (2022).
301. Wu, H. et al. The field-free Josephson diode in a van der Waals heterostructure. *Nature* **604**, 653–656 (2022).
302. Teng, X. et al. Discovery of charge density wave in a kagome lattice antiferromagnet. *Nature* **609**, 490–495 (2022).
303. Zhang, H. et al. Exchange-biased topological transverse thermoelectric effects in a kagome ferrimagnet. *Nat. Commun.* **13**, 1091 (2022).
304. An, Y. et al. Topological and nodal superconductor kagome magnesium triboride. *Phys. Rev. Mater.* **7**, 014205 (2023).
305. Huang, J. et al. Three-dimensional flat bands and Dirac cones in a pyrochlore superconductor. Preprint at https://doi.org/10.48550/arXiv.2304.09066 (2022).
306. Deng, L. Z. et al. Magnetic kagome superconductor $CeRu_2$. Preprint at https://doi.org/10.48550/arXiv.2204.00553 (2022).
307. Ku, H. C., Meisner, G. P., Acker, F. & Johnston, D. C. Superconducting and magnetic properties of new ternary borides with the $CeCo_2B_2$-type structure. *Solid. State Commun.* **35**, 91–96 (1980).
308. Escorne, M., Mauger, A., Gupta, L. C. & Godart, C. Type-II superconductivity in a dilute magnetic system: $La_{1-x}Tm_xRu_3Si_2$. *Phys. Rev. B* **49**, 12051–12057 (1994).
309. Chaudhary, S. et al. Role of electronic correlations in the kagome-lattice superconductor $LaRh_3B_2$. *Phys. Rev. B* **107**, 085103 (2023).
310. Ye, L. et al. Massive Dirac fermions in a ferromagnetic kagome metal. *Nature* **555**, 638–642 (2018).
311. Lin, Z. et al. Flatbands and emergent ferromagnetic ordering in Fe_3Sn_2 kagome lattices. *Phys. Rev. Lett.* **121**, 096401 (2018).
312. Barz, H. New ternary superconductors with silicon. *Mat. Res. Bull.* **15**, 1489–1491 (1980).
313. Malik, S. K., Umarji, A. M., Shenoy, G. K., Aldred, A. T. & Niarchos, D. G. Magnetism and superconductivity in the system $Ce_{1-x}La_xRh_3B_2$. *Phys. Rev. B* **32**, 4742–4745 (1985).
314. Li, S. et al. Anomalous properties in the normal and superconducting states of $LaRu_3Si_2$. *Phys. Rev. B* **84**, 214527 (2011).
315. Gruner, G. The dynamics of charge-density waves. *Rev. Mod. Phys.* **60**, 1129 (1988).
316. Gruner, G. The dynamics of spin-density. *Rev. Mod. Phys.* **66**, 1 (1994).
317. Fradkin, E. in *Modern Theories of Many-Particle Systems in Condensed Matter Physics* 53–116 (Springer, 2012).
318. Kivelson, S. A., Fradkin, E. & Emery, V. J. Electronic liquid-crystal phases of a doped Mott insulator. *Nature* **393**, 550–553 (1998).
319. Agterberg, D. F. et al. The physics of pair-density waves: cuprate superconductors and beyond. *Annu. Rev. Condens. Matter Phys.* **11**, 231–270 (2020).

Acknowledgements
Y.W. acknowledges support from NWO Talent Programme Veni financed by the Dutch Research Council (NWO), project no. VI.Veni.212.146. H.W. acknowledges support from the Kavli Institute of Nanoscience Delft Synergy grant 2022. Y.W., H.W. and M.N.A. acknowledge support from the Technical University of Delft Quantum Nanoscience Department as well as the Kavli Institute of Nanoscience Delft. J.Y.C. acknowledges NSF-DMR 2209804 and Welch AA-2056-20220101 for partial support of this work.

Author contributions
Y.W. and H.W. wrote the majority of the manuscript. M.N.A. and J.Y.C. are the principal investigators. All authors contributed to the writing of the manuscript.

Competing interests
The authors declare no competing interests.

Additional information
Peer review information *Nature Reviews Physics* thanks Hu Miao, Fazhi Yang and the other, anonymous, reviewer(s) for their contribution to the peer review of this work.